# MODEL BASED DESIGN AND EVALUATION OF MEASUREMENT SYSTEMS

By

Joseph Thomas Howard

Dissertation

Submitted to the Faculty of the

Graduate School of Vanderbilt University

in partial fulfillment of the requirements

for the degree of

DOCTOR OF PHILOSOPHY

in

Mechanical Engineering

December 16, 2023

Nashville, Tennessee

Approved:

Eric Barth, Ph.D.

Jason Mitchell, Ph.D.

Michael Goldfarb, Ph.D.

Arthur Witulski, Ph.D.

Brett Byram, Ph.D.

## TABLE OF CONTENTS

## LIST OF TABLES

## LIST OF FIGURES

# CHAPTER 1

# Introduction

## 1.1 Motivation

In the ever-evolving landscape of engineering, accurate and reliable measurement systems serve as the bedrock upon which countless innovations and technological advancements are built. As modern engineering challenges grow more complex, the demand for novel methods of sensing the world around us and more accurate models to explain that world grow in tandem.

This dissertation delves into the realm of both model-based design and sensor evaluation, with a particular emphasis on physics-based models in the design and evaluation of measurement systems. Through a combination of theoretical principles, practical applications, and empirical studies, this research aims to advance the state of the art in radiation tolerant robotics, underwater imaging, and artificial hearts. The journey begins by proposing a method to evaluate an encoder's performance in a high-radiation environment, traversing through the development of an acoustic model to inform the design of a novel short-range sonar system, and culminating in the translation of a lumped parameter model of the human circulatory system into the physical domain. As the following chapters unfold, the dissertation seeks to contribute to the pursuit of precision and reliability in both measurement and modeling, enabling engineers, scientists, and industries to push the boundaries of what is achievable.

### 1.1.1 On the Applications of Radiation Tolerant Robotics

In 2011, a tsunami hit the coast of Japan, resulting in the meltdown of the Fukushima Daiichi Nuclear Power Plant. In the days, months, and years following the incident, numerous robots used to survey the damage experienced failures resulting in the loss of control. Though significantly less susceptible to radiation than humans, robots are not immune to radiation damage. Ionizing radiation damages circuitry within sensors which can severely impact sensing ability, and by extension, feedback loops and movement.

In any emergency situation, especially one nuclear in nature, the rapid deployment of robots is advantageous for search & rescue operations, damage control, and situation monitoring. The more widespread these "first responder" robots are, the faster they can be deployed. It is beneficial, therefore, to work toward robots with modern dexterity developed with commercially available components, yet whose performance degrades gracefully when exposed to ionizing radiation rather than outright loss of control.

### 1.1.2 On the Applications of Short-Range Sonar

Divers frequently inspect and perform repairs on ocean structures, dam infrastructure, and ship hulls underwater. These efforts are difficult in regions of high turbidity where murky water prevents visual inspection, forcing divers to rely on touch-based inspection instead. According to the United States Navy, a military diver carries out nearly all their work in zero visibility, never actually seeing their underwater worksites [2]. Many Navy divers indicated that sonar imagery should be a priority when interviewed about a candidate heads up display [3]. A device that can help a diver maintain vision in zero-visibility would dramatically improve the diver's effectiveness, allowing for faster repairs and more complete inspections.

### 1.1.3 On the Importance of Artificial Heart Development

According to 2018 data from the Center for Disease Control (CDC), heart disease affected 10.7% of adults in the United States and accounted for 22.6% of the annual deaths [4, 5]. For people living with advanced heart disease, a cardiac transplant is often the treatment of choice when all other options have been exhausted. Unfortunately, donor hearts are very rare, with the annual number of heart transplants in the United States plateaued at less than 3000 per year [6]. Total Artificial Hearts (TAH) and Ventricular Assist Devices (VAD) seek to solve this shortage by replacing or assisting a failing heart with a mechanical pump. Currently, both devices are used as a bridge to transplantation for patients with end-stage heart failure, but artificial heart developers are working on devices suitable for permanent heart replacement. With modern advances in power dense motors and compact energy storage, as well as recent innovations in compact pump designs, there are several devices in development that promise to mitigate complications associated with current devices while providing the reliability needed for a permanent replacement.

## 1.2 Background

### 1.2.1 Radiation Effects on Sensors

There are two classes of radiation effects on electronics relevant to sensors, Single Event Effects (SEE), and Total Ionizing Dose (TID). Single Event Effects are transient and are caused by a single charged particle as it passes through a semiconductor. Low reaction energies can cause "soft" errors that can flip memory bits or cause communication errors, while high reaction energies can destroy systems by permanently latching switching systems or rupturing transistor gates. While SEE is primarily a transient event, Total Ionizing Dose is cumulative damage due to the ionization of semiconductor material. Transistors exposed to this damage experience threshold shifts, increased leakage current, and changes in switching times. In the context of sensors, transistors are responsible for amplifying signals to transmission levels, comparing output, and on-chip signal analysis. Additionally, the same effects that cause transistor degradation can also cause changes

in the sensing mechanism itself. Changes in both transistor and sensor parameters can cause a sensitivity shift before the device succumbs to total failure.

The 2011 Fukushima disaster showed that robots are not prepared for traversing a damaged power plant with high radiation levels. Robots with the dexterity required to navigate such a complex environment had their sensors succumb to radiation damage, both leaving the mission incomplete and adding a new obstacle for the next robot scout. While radiation hardened electronics exist for robotic applications in harsh environments, they rely on extremely expensive components whose performance is significantly worse than modern commercial parts.

Since sensors tend to degrade before outright failure, it is possible to develop a new class of robots, radiation tolerant, that while not fully hardened, can survive longer due to improved control robustness. With the goal of improving first responders' access to search & rescue robots for a nuclear emergency, it is better to widely distribute modified Commercial Off the Shelf (COTS) robots with some radiation tolerance than to strategically pinpoint a few fully radiation hardened robots. Work in this dissertation is toward evaluating the effectiveness of a robot to withstand radiation and offer design suggestions to improve its tolerance.

There is a substantial body of work evaluating the radiation tolerance of mission-critical electronics, including sensors, for spacecraft. However, these devices are evaluated on a pass/fail basis for a radiation level defined by a specific mission. Designing a robotic system robust to hostile environments requires quantifying how feedback sensors react to such environments. Then the control system can be designed to operate even as sensors degrade. Therefore, this dissertation aims to develop analysis techniques to detect errors in a sensor's data stream and quantify the sensing changes relevant to robotic control stability.

### 1.2.2 Providing Vision in Zero Visibility Diving Conditions

The emergence of heads-up displays in glasses provides new opportunities for conveying information to professionals on location. The United States Navy has experimented with integrating a heads-up display into a diving helmet to convey data relevant to inspection, repair, and search tasks [3]. A prototype device displayed sector sonar images, high-resolution sonar video, navigational aids, and text with basic dive information to the wearer. This information is still readable in zero-visibility conditions because it displayed completely within the helmet.

The logical progression of this technology is to help a diver maintain spatial awareness in zero-visibility conditions by mapping and displaying his surroundings in real time. Most spatial mapping techniques used in robotics are unsuitable for this application, as turbid water conditions are opaque to visual and near-visual light preventing the use of stereo cameras and LIDAR, and water's high absorption of electromagnetic (EM) radiation, including microwaves and radio waves precludes radar mapping techniques. Underwater acoustic

imaging has a decades-long successful history of submarine navigation and ocean terrain mapping. Short-range sonars exist and can be hand-held or mounted to Remotely Operated Vehicles (ROV). These devices can provide an overview of a large area, but lack the resolution needed for detailed inspection and depth of field appropriate for work within arm's reach. Medical ultrasound regularly takes images through visually opaque materials at the resolutions required to map an environment for inspection and repair, albeit with substantially different range and size requirements. Therefore, this dissertation aims to augment a medical-class ultrasound transducer's capabilities using clever hardware design to match the requirements of this more demanding use.

### 1.2.3 Improving Artificial Heart Development with Dynamically-Accurate Loads

Currently, only one Total Artificial Heart exists on the market that is FDA approved for total heart replacement. Due to long-term reliability concerns, this approval is only for a temporary replacement until a suitable biological heart becomes available. With modern advances in power dense motors and compact energy storage, as well as recent innovations in compact pump designs, the artificial heart scene is ripe for innovation.

Recent studies suggest that pulsatile blood flow is important to maintain physiological homeostasis [7], so the dynamic flow characteristics of candidate artificial hearts must be tested with a realistic hydraulic load. Some labs developing artificial hearts have Mock Circulatory Loops (MCL) with actual blood to order to evaluate the pump's overall compatibility with blood. Testing with blood will always be a vital part of the design process, but a more accessible and biohazard-free loop would be more conducive to rapid design-prototype-test phases in an engineering lab. Other labs use dynamically simple MCLs for constant flow Ventricle Assist Devices (VAD), but these lack the dynamics required for designing and testing pulsitile devices. It is critical, then, to fill the gap between *in silico* simulation and full-blown *in vitro* testing. Tuning a pump's pulsitility through both hardware design and embedded control require a realistic test stand that can support frequent modifications to the pump.

## 1.3 Dissertation Contributions

The following dissertation contains three chapters whose primary contributions are as follows:

Chapter 2 outlines the development of a hardware system and statistical method to identify the effect of radiation on an electromechanical sensor. Constraints on testing methodology introduced measurement uncertainty on the same order of magnitude as the observed radiation effects, which this work successfully differentiates between.

- Develops testing methodology and hardware to expose a COTS encoder to ionizing radiation while minimizing positional variation

- categorizes all sources of measurement error and quantifies a total uncertainty through statistical analysis
- Quantifies sensitivity changes at various levels of Total Ionizing Dose, and provides recommendations for robotic control design to tolerate these changes

Chapter 3 details the development of the first prototype for a short-range, high-resolution, head-mountable sonar device for underwater inspection and maintenance tasks in zero-visibility conditions. The system features an ultrasound imaging sensor and novel curved acoustic mirrors for beam focusing. It also proposes characterizing the system's elevational resolution using pressure field measurements from both simulation and physical hardware.

- Develops hardware to support the in-demand yet currently unfilled niche for mapping solid surfaces with sonar
- Proposes a novel ultrasound focusing method utilizing curved acoustic mirrors rather than typical phased-array beamforming or acoustic lenses
- Develops a complete simulation of the device, modeling the interaction between the acoustic mirrors and both the transmitted beam and the received scattered signal
- Validates simulation by measuring the acoustic field from physical hardware
- Demonstrates the system's ability to take an acoustic image at the focal point with under 3.0mm resolution

Chapter 4 proposes a Mock Circulation Loop (MCL) to support the development of artificial hearts. This test load accurately mimics the dynamic impedance of the human circulatory system and is designed to be the first load connected to a prototype device to both evaluate a pump's inherent pulsatility and develop a flow controller.

- Compares the simulation performance of multiple lumped parameter models and multiple parameter sets common in literature
- Proposes a novel hardware design to recreate the best performing lumped parameter model in the hydraulic domain
- Fabricates the design and experimentally validates dynamic parameters of the hardware using system identification

# CHAPTER 2

## Isolation of Radiation Effects from Mechanical and Control Uncertainty Sources

Portions of this text previously appeared in:

**J. T. Howard**, E. J. Barth, R. D. Schrimpf, R. A. Reed, L. C. Adams, D. Vibbert, A. F. Witulski, "Methodology for Identifying Radiation Effects in Robotic Systems With Mechanical and Control Performance Variations," in IEEE Transactions on Nuclear Science, vol. 66, no. 1, pp. 184-189, Jan. 2019.

**J. T. Howard**, E. J. Barth, R. D. Schrimpf, R. A. Reed, D. Vibbert, A. F. Witulski, "Methodology for Identifying Radiation Effects in Robotic Systems with Mechanical and Control Performance Variations," IEEE Nuclear and Space Radiation Effects Conference (NSREC), July 2018.

### 2.1 Introduction

Modern robotics requires fast and accurate sensing of both the robot and its operating environment for feedback control. These sensors can degrade in a total ionizing dose (TID) radiation environment such as radiation contamination in a power plant. However, reliably distinguishing between radiation degradation and normal device operational variation in laboratory tests is more difficult with electromechanical sensors than with purely electronic devices. Mechanical stimuli have non-negligible variation primarily due to alignment aspects of the test fixture. This work presents a method for distinguishing radiation degradation in electromechanical sensors from normal operating variations by applying uncertainty analysis to the pre-radiation and post-radiation data sets.

The 2011 Fukushima-Daiichi accident saw the use of robots to survey the damage [8, 9]. While fully custom designs are necessary for operation near radiation sources [10], commercial search and rescue robots are useful for rapid-response survey missions. General purpose search and rescue robots such as DARPA's ATLAS humanoid robot owe their dexterity to state-of-the-art commercial off-the-shelf (COTS) parts. COTS components are composed of complex circuits with many subsystems on the same die that cannot be separated into different packages for analysis or testing. The only inputs to advanced sensor ICs are the mechanical properties (acceleration, etc.) that the sensors measure, and the only outputs are analog or digital waveforms representing the often highly processed data. Diagnostic pins are rarely found on modern sensor ICs so there is no window into their complex inner workings. This hidden complexity makes it difficult to build analytical radiation models of the sensors. Figure 2.1 shows an example of such complexity between inputs and outputs in a Hall Effect encoder IC. Notice that in addition to the Hall Elements themselves, the die also contains analog amplifiers, analog to digital converters, and an application specific digital computer. Encoders are

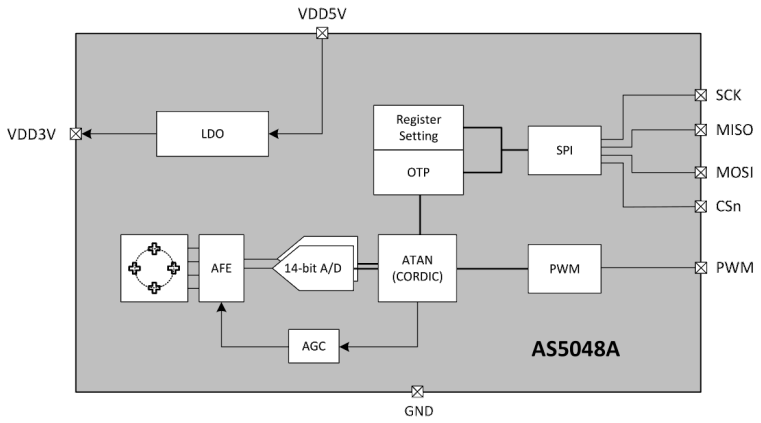


Figure 2.1: Functional block diagram of the Hall Effect rotary encoder used for testing [1]

essential feedback sensors for robots that provide joint angle feedback to the control system.

Previous work has shown that a robotic system can still accomplish its task while the sensor is degrading due to TID but before total failure occurs [11, 12]. Statistical models can predict how the system responds to different TID levels when there is a model for the sensor's degradation [13]. Previous works have validated individual hall elements as proximity sensors for spacecraft use, not exceeding mission specifications for sensitivity changes up to 30 krad(Si) [14] and 40 krad(Si) [15]. The samples in [14] failed to operate past 50 krad(Si) while the samples in [15] were not tested to failure. Another work validated a fully custom radiation hardened Hall Effect encoder IC up to 100 krad(Si) with a maximum positioning error of 1.5° [16]. A study of the degradation region for accelerometers [11] and range finding sensors [13] has been completed, but few other works have explored measurement sensitivity changes due to TID.

A COTS contactless Hall Effect rotary encoder is used to illustrate how to isolate radiation-induced changes in measurement sensitivity from normal variation in sensor operation. In order to quantify what constitutes as normal measurement variation, one must consider sources of random and systematic errors in measurements of mechanical quantities. Random error is typically a result of amplified electrical noise and is dealt with by collecting a large number samples. Systematic error is typically due to uncertainty in the input/output (IO) calibration between the sensor's transducer and output due to (1) unmodeled transducer nonlinearities, and (2) changes in the sensor's mechanical positioning during a test. In this paper we describe an uncertainty quantification approach that is used to measure changes in expected output with an uncertain but predictable input.

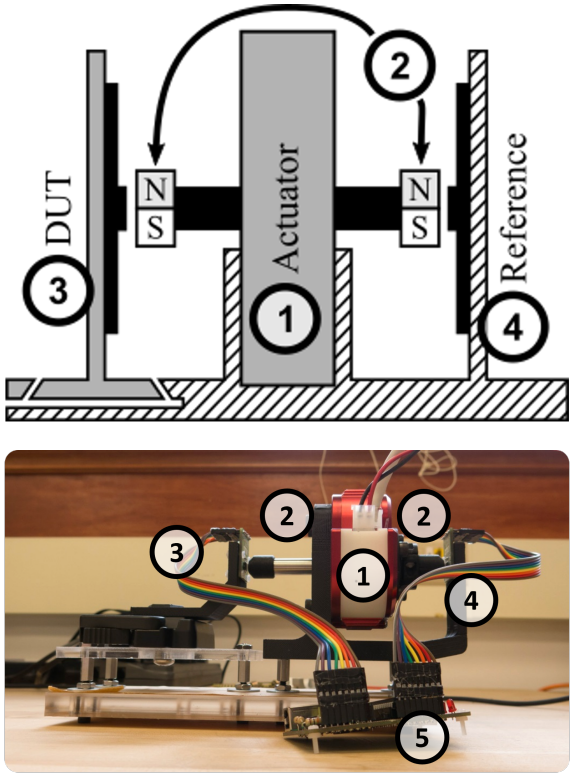


Figure 2.2: Schematic and photograph of the test fixture showing: 1) HEBI actuator (motor and controller), 2) magnet end mounts, 3) removable DUT sensor, 4) fixed reference sensor, 5) custom DAQ board.

### 2.2 Experimental Setup

To demonstrate the use of this methodology, this paper uses the Hall Effect absolute encoder in Figure 2.1 (AS5048A manufactured by Austria Microsystems) as a case study. This IC was chosen because of its widespread use in commercial robotic systems. This is a COTS part with a number of subsystems on the same die, including a Hall Effect magnetic sensor array, an analog-to-digital converter, and a digital hardware implementation of the coordinate rotation digital computer (CORDIC) arctan algorithm. There are two communication busses to transmit the same information, a pulse width modulated (PWM) output with a duty cycle proportional to the angle, and a serial peripheral interface (SPI) bus. The magnetic field orientation from a magnet mounted on a motor shaft is the only input other than DC power and the PWM and SPI are the only outputs. Both the SPI and PWM interfaces report the orientation of the magnetic field as a proportion of a full rotation.

As shown in Figure 2.2, the test setup consists of a velocity-controllable motor (X5 actuator by HEBI Robotics) connected to a through-shaft for repeatable positioning of the device under test (DUT) and reference sensor. The ends of the shaft have identical diametrically polarized magnets attached in approximately the same orientation. Radiation test data cannot be collected inside an irradiator because the mechanical test

equipment would block a direct line-of-sight from DUT to radiation source. The fixture has a removable bracket to allow the DUT to move between the irradiator and the fixture. The removable bracket is held in place with spring-loaded wedge (camera tripod quick release) while the reference sensor is fixed with respect to the motor to minimize sensor placement variation. During a test, the motor is run with a constant velocity command to rotate the permanent magnet and therefore the magnetic field measured by the encoder. The actual velocity, however, is not constant due to physical and control-related limitations. In addition to the mechanical fixture, a custom data acquisition solution was developed to read both the SPI and PWM outputs of both the DUT sensor and the reference sensor. The system is able to sample at 1.25 kHz, which is sufficient for mechanical response timescales. A Test Run is defined as a test where the DUT is locked into the fixture and the magnetic field is rotated through three complete revolutions. During this run, data points are collected at the DAQ's maximum 1.25 kHz sampling rate. This test methodology requires Calibration Runs, which are pre-radiation Test Runs used to measure the variation due the test fixture's mechanical tolerance. The DUT must be removed and re-inserted between each Calibration Run.

### 2.3 Data Analysis

A measurement taken from the fixture can be modeled as a sum of the true angular position of the magnetic field plus errors due to the fixture, nonlinearity, and radiation effects:

$$M = \theta_{true} + E(\theta) + S(\theta) + R(\theta) \tag{2.1}$$

where $M$ is the measurement, $E$ is the fixture alignment error, $S$ is the sensor's pre-radiation nonlinearities, and $R$ is the sensitivity change due to radiation. This model captures all systematic errors such as multiplicative effects (e.g. $3(4) = (4) + 8$ or linear offsets in sensitivity by modelling $E$, $S$, and $R$ as functions of angular position. Figure 2.2 shows a model overview for measuring a motor's shaft with an affixed permanent magnet using two sensors.

The true angular position, $\theta_{true}$, is unknown because the motor dynamics do not follow the velocity target perfectly. The $\theta_{true}$ term is removed by subtracting the Reference sensor measurement, $M_B$, from the DUT measurement, $M_A$. Since the reference measurement, $M_B$, does not contain radiation effects, the resulting expression has only the radiation effect term from $M_A$. Solving the expression for the radiation effect found in $M_A$ results in the following expression:

$$R(\theta) = (M_A - M_B) - (E_A(\theta) - E_B(\theta) + S_A(\theta) - S_B(\theta)) \tag{2.2}$$

$$= (M_A - M_B) - C(\theta) \tag{2.3}$$

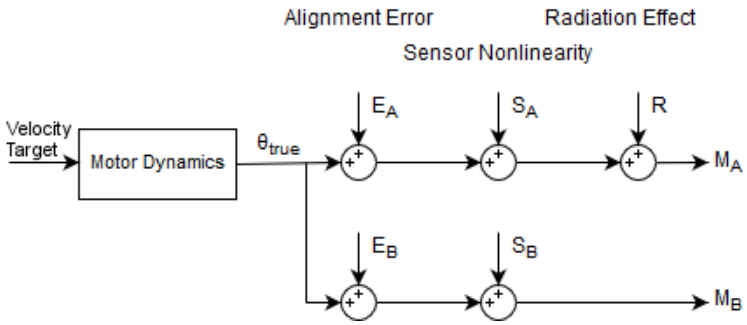


Figure 2.3: Block diagram illustrating sources of measurement error for angular displacement of motor shaft, using an irradiated DUT (A) and a non-irradiated Reference sensor (B)

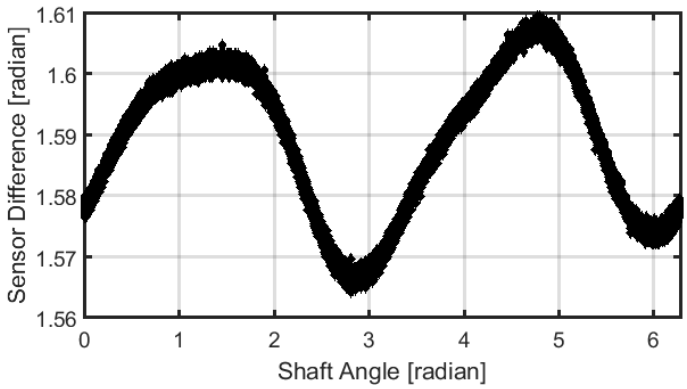


Figure 2.4: Sample plot showing $C = (M_A - M_B)$ vs shaft angle for a single pre-radiation test run. Statistics are calculated by dividing the x axis into n bins and computing the mean and variance for each bin.

The calibration factor, $C$, includes extrinsic fixture misalignments, $E$, and intrinsic sensor nonlinearities, $S$, for both sensors. This factor's expected value and corresponding error bars can be found at each angle of the shaft rotation through pre-radiation testing of the DUT, that is, when $R = 0$. If the Reference sensor is permanently attached to the fixture, then the transformation between $\theta_{true}$ and $M_B$ is consistent, allowing the approximation of $C(\theta)$ and $R(\theta)$ as $C(M_B)$ and $R(M_B)$, respectively. Figure 2.4 shows a sample calculation of $(M_A - M_B)$ from a test run where the sensor's input is swept across the sensing range 3 times. This pre-radiation calibration process was repeated 15 times for each sensor in this work. The DUT must be fully removed from and reseated in the fixture between each calibration run to fully characterize the misalignment.

Pre-radiation measurements are then grouped into n bins with respect to measured shaft rotation in order to directly compare pre- and post-irradiation runs. Bins should be selected such that there are greater than 30 data points in each bin so the Gaussian z-statistic may be used in the statistical analysis described later.

The statistical analysis takes the form of a 2-mean hypothesis test where the null hypothesis is $A - B = 0$ [17]. Note that this is the same form as Equation 2.3. Recall that a statistical hypothesis test requires construction of a critical region based on the combined errors in the collected data. There are 3 quantifiable

sources of error in this form.

$$u_1 = t_{99\%,m-1}\frac{\sigma_C}{\sqrt{m}} \tag{2.4}$$

$$u_2 = z_{99\%}\frac{\sigma_T}{\sqrt{f}} \tag{2.5}$$

$$u_3 = \frac{z_{99\%}}{m}\sum_{k=1}^{m}\frac{\sigma_k}{\sqrt{l_k}} \tag{2.6}$$

Equation 2.4 is the alignment error in the calibration curve, which is calculated using the standard deviation of the measured $C$, $\sigma_c$, for all calibration runs 1 through $m$. Since there were fewer than 30 calibration runs taken in this work, the Student's T Statistic is used in accordance with statistical best practices for 99% confidence. Equation 2.5 is the error in the mean of the test run, $\sigma_T$, which is calculated simply using the standard deviation of points within each bin of a post-radiation test. The number of points in the bin, $f$, was chosen to include more than 30 points so the z-statistic is used. Equation 2.6 is the sensitivity of the calibration curve to noise, which is a result of $\bar{C}$ being a function of measurements.

$$\bar{C} = \frac{c_1 + c_2 + ... + c_m}{m} \tag{2.7}$$

According to standard instrumentation practices [18], the error of a value calculated using measurements is

$$dy = \frac{\delta f}{\delta x_1}dx_1 + \frac{\delta f}{\delta x_2}dx_2 + \cdots + \frac{\delta f}{\delta x_n}x_n \tag{2.8}$$

where $x1 \ldots xn$ are measurements with error and y is a value calculated using the measurements. Applying this method of error propagation to $\bar{C}$ results in the uncertainty due to signalling noise.

$$u_3 = \sum_{k=1}^{m}\frac{\delta\bar{C}}{\delta C_k}\cdot z_k\frac{\sigma_k}{\sqrt{l_k}} \tag{2.9}$$

where $\sigma_k$ is the standard deviation of, and $l_k$ is the number of points in, the $k$th pre-radiation calibration run. Since $\bar{C}$ consists of a sum of independent variables divided by a constant, the partial derivative of Equation 2.7 with respect to each variable is equivalent.

$$\frac{\delta\bar{C}}{\delta C_1} = \frac{\delta\bar{C}}{\delta C_2} = ... = \frac{\delta\bar{C}}{\delta C_m} = \frac{1}{m} \tag{2.10}$$

If each bin size is chosen to include more than 30 points, then the z-statistic is the same for each error source

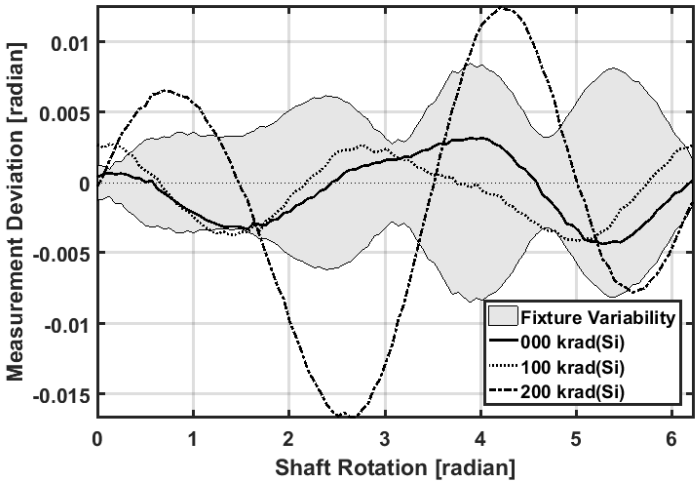


Figure 2.5: Detail of Sensor 5 (Date Code 1, X-Ray Source) response at different TID.

in Equation 2.9.

$$z_1 = z_2 = \cdots = z_k \tag{2.11}$$

Note that if bins are not chosen to include more than 30 points, then Equation 2.11 does not hold and individual T-statistics should be used instead. The relationships in Equations 2.10 and 2.11 allow Equation 2.9 to be simplified to Equation 2.6. A final fixture variability envelop is calculated using the Kline-McClintok equation [15] to combine all three sources of error,

$$FixtureVariabilityEnvelope = \pm\sqrt{\left(t_{99\%,m-1}\frac{\sigma_C}{\sqrt{m}}\right)^2 + \left(z_{99\%}\frac{\sigma_T}{\sqrt{f}}\right)^2 + \left(\frac{z_{99\%}}{m}\sum_{k=1}^{m}\frac{\sigma_k}{\sqrt{l_k}}\right)^2} \tag{2.12}$$

where the standard deviation in the bin of the $k$th calibration run is $\sigma_k$, the standard deviation in the averages of calibration runs is $\sigma_C$, and the standard deviation of the test run is $\sigma_T$. The number of samples in the bin for the $k$th calibration run is $l_k$, the number of samples in the bin for the test run is $f$, and the number of calibration runs is $m$.

### 2.4 Experimental Results

Six total devices were tested for sensing degradation due to TID. Sensors 1, 2, and 3 were tested in a 660 keV $^{137}$Cs gamma irradiator. Sensors 4, 5, and 6 were decapsulated and tested in a 10-keV X-Ray irradiator. The X-Ray source allowed higher doses due to its higher dose rate, but the lower penetration energy required the silicon die be exposed prior to testing. Sensors 1-4 were manufactured in week 21 of 2013 (date code 1) and Sensors 5 and 6 were manufactured in week 40 of 2015 (date code 2).

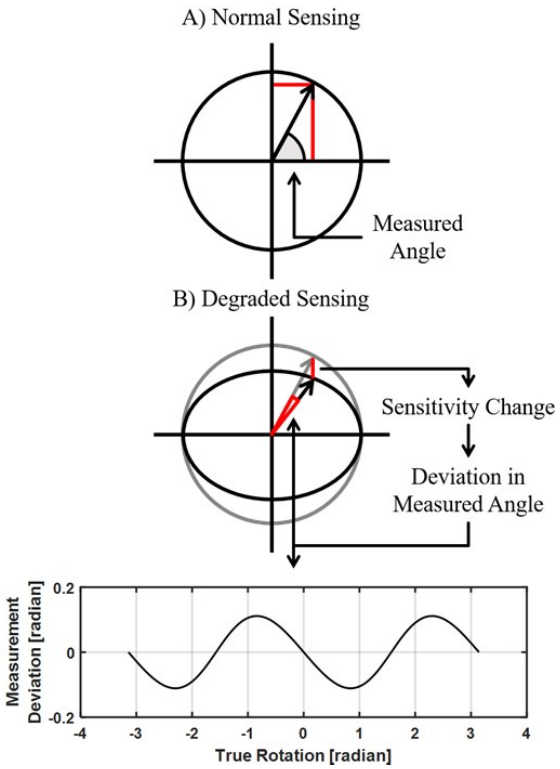


Figure 2.6: The effect of hall element sensitivity change on angle measurement

Sensor 5 (date code 2, X-Ray source) showed the greatest deviation due to radiation in absolute positioning accuracy with a change in 0.01 radians (approximately 0.5°) outside the fixture variability envelope. Figure 2.5 shows the difference in measurement from the device's pre-radiation calibration at increasing TID. This figure also plots the fixture variability envelope in order to tell if the difference is within pre-radiation variation.

In robotics, an encoder's rate of change is often used to calculate the joint velocity in a proportional-integral-derivative controller (PID). Therefore, the slope of the deviation curve is an important metric. Over the range of 2.70 to 4.27 radians, a change in $\pi/2$, the deviation from pre-radiation performance goes from -0.017 to 0.012. This means that joint velocities measured by this sensor in this range would be 1.5% higher than the true joint velocity. A variation of this magnitude could cause undesirable performance or instability at rate feedback gains otherwise considered reasonable.

While there is little that can be done to extend the life of the highly-integrated COTS IC itself, the useful life of the whole robotic system can be improved by designing a motion controller to be robust to the sensitivity changes that occur before outright sensor failure. In this particular case, the measured radiation effect could cause undesirable robotic performance in precise and/or fast positioning applications. Both the maximum position error and velocity measurement error can be used by roboticists to inform controller

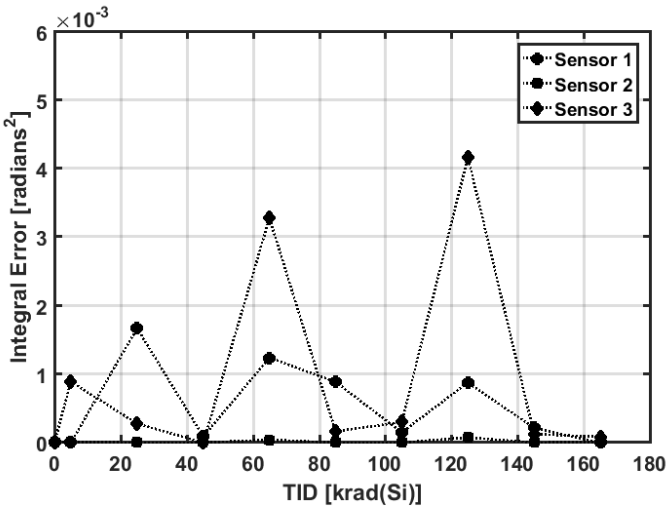


Figure 2.7: The area between the measurement deviation curve and outside of the fixture variability boundary plotted against TID.

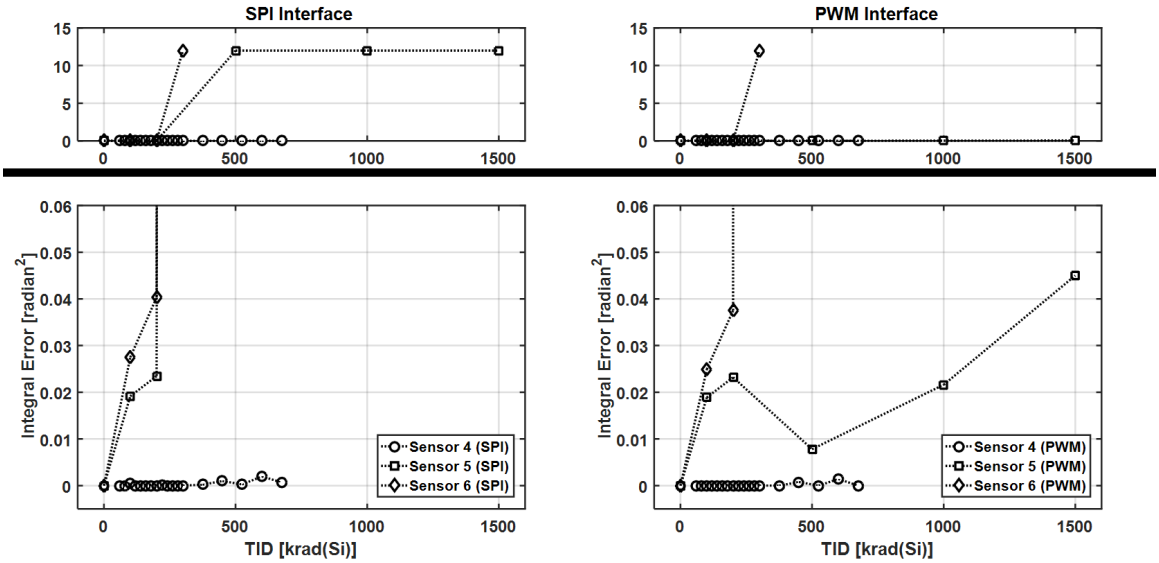


Figure 2.8: SPI and PWM interface total integrated error at different TID levels.

requirements to ensure systems-level stability.

It is difficult to extract a definitive physical explanation of the post-radiation behavior because there is no access to the IC's internal signals. However, this behavior is consistent with a change in Hall unit sensitivity and/or a change in amplification gain. The IC feeds two amplified differential signals from two pairs of Hall elements to a digital hardware implementation of the ARCTAN function called CORDIC. As seen in Figure 2.6, a linear change in sensitivity or amplification in one direction results in periodic, nonlinear measurement deviation similar to that seen in Figure 2.5.

The data shown in Figure 2.5 can be compressed to a single data point by taking the total area outside the

expected deviation area. As the sensor continues to degrade, the metric penalizes both proportion of sensing range spent outside the pre-radiation tolerances and high magnitudes of sensor deviation.

Three sensors of the same date code were tested with a Cesium source. The integrated error for each sensor with respect to TID shows a non-monotonic response to TID in Figure 2.7. This type of non-monotonic behavior is to be expected from a complex sensor system-on-a-chip with error compensation techniques built into the system. The fully custom, radiation hard Hall Effect based encoder in [16] also exhibited similar non-monotonic behavior with increasing TID with positioning error fluctuating around pre-radiation values.

Three additional sensors were delidded and tested in an X-Ray source. Both Sensors 5 and 6 (date code 2) experienced SPI communication bus failure between 200 and 300 krad(Si). Sensor 6 also lost the PWM interface at the same time while Sensor 5 continued communicating over PWM until testing was stopped at 1500 krad(Si). Sensor 4 (date code 1) continued to communicate over its SPI bus through 675 krad(Si).

Figure 2.8 shows that The first column shows errors over the SPI interface. The second column shows the PWM interface. For both columns, the top plot shows are wider range of integral error, and the bottom plots show detail near zero. It can be seen that sensor 4 maintains communication across the TID range tested, while sensor 5 maintains PWM communication with only small errors but fails SPI communication after 675 krad(Si), and sensor 6 effectively fails in SPI and PWM communication between 200 and 300 krad(Si). Interestingly, even after the SPI bus failed in Sensor 5, the integrated position error from PWM interface remains within the same order of magnitude for the entire TID range tested. This suggests that the majority of the sensing circuitry is relatively radiation-tolerant compared to many COTS parts.

The SPI bus failure in sensors 5 and 6 suggests that abrupt SPI communication bus failure is likely to be the cause of system-level failure rather than degraded sensing.

## 2.5 Summary

As more complicated sensors make their way into high radiation environments, engineers require more complicated methods of measuring the effect on their outputs when exposed to ionizing radiation. The integrated circuit tested in this work is no exception. To test for sensitivity changes, it required a known rotary input to compare measured outputs against one another. This unique input requirement necessitated a test stand allowing for the removal and accurate replacement of the sensor, significantly more complicated than is typically used in radiation testing and validation.

The uncertainty of sensor placement relative to the input, and by extension, uncertainty of the input to the sensor itself, resulted in output uncertainty of a similar magnitude to the sensitivity change due to radiation. The expected variation in measurement deviation due to fixture variation was calculated for multiple positions by utilizing several calibration runs prior to irradiation. Any measurement deviation that fell outside of the

uncertainty region is therefore likely caused by ionizing radiation damage.

This methodology provides a means to extract radiation effects from an electromechanical sensor using measurements of a mechanical quantity. This methodology goes beyond a simple pass/fail criterion by providing insight into TID's effect on the magnitude of change experienced.

This particular sensor had a maximum sensing deviation of 0.5° and a maximum velocity deviation of 1.5% due to TID. This work suggests that a robotic control algorithm based on this particular sensor is unlikely to be affected by the sensitivity changes due to TID. Rather, this sensor's abrupt communication failure is more likely to cause a loss of feedback control. Therefore, efforts to increase the radiation tolerance of systems built around this sensor should address the sudden loss of a feedback sensor by estimating the missing channel through other sensors and knowledge of the system dynamics. Although the sensor in this work experienced little sensitivity changes, other sensors may be more affected by TID resulting in greater sensing deviations. The method outlined in this work can be used to measure these effects on a whole class of sensors that measure a physical quantity.

Ultimately, quantities needed to inform requirements in robotic controller design were isolated with statistical confidence despite both nonlinear sensitivity changes due to TID and parasitic variation due to testing constraints.

### 2.6 Future Directions

It is possible to apply the method of quantifying the alignment uncertainty to quantify sensitivity changes to a a whole class of sensors that measure physical quantities. Maximum deviations in sensitivity can set requirements on control robustness for systems.

For feedback control systems based on this particular sensor, TID is more likely to cause the sudden failure of the communication busses of this encoder than sensitivity changes significant enough to cause loss of control. Therefore, the next step for this sensor is to develop control strategies that can withstand sensor channel dropout. Sensor fusion and observer based controllers can estimate unmeasured states using measurements of different quantities and knowledge of the system's dynamics. A potential area of study is to extend these methods by adding knowledge of the specific task. For example, the future states of a robotic manipulator performing a repetitive task, such as taking a material sample for analysis, can be predicted by it's past past states. Including knowledge of both the dynamics and the task may reduce the number of independent states compared a dynamic model alone, thus improving the model's ability to predict states, and therefore retain feedback control, with limited information.

An interesting observation, though not previously discussed, is that the COTS IC tested in this work withstood significantly higher TID than other COTS ICs like the accelerometer [11] or rangefinder [13]. One

possible explanation for how this encoder's sensing remained largely intact is how the encoder rejects the background magnetic field applied to the whole IC. Differential signals between pairs of hall elements are fed into the angle calculating circuitry. This effectively removes the effect of the environment's magnetic field resulting in a measurement of only the field from the magnet whose orientation it is measuring. If the individual hall sensors were to degrade similarly with the same TID, the effect on sensing may be functionally similar to an environmental magnetic field and would be removed due to it's design. This is difficult to impossible to prove without access to the IC's internal signals, so it was not mentioned in the previous sections. Regardless of the actual explanation for this IC's remarkable resilience to TID, this leads to the idea of a system-level design where feedback is some delta between two sensors exposed to the same environment, and thus degrading similarly. For instance, taking the difference between readings of two accelerometers mounted in opposing orientations would result in double the true acceleration vector, reducing zero-point drift through system-level design. While this by no means guarantees functionality during sensitivity degradation since no two sensors will degrade identically, but this could be a promising method of radiation tolerant design strategy for sensors with similar degredation characteristics, and deserves further study.

# CHAPTER 3

## Development of a Short-Range, High-Resolution Sonar

The device described in this chapter is patent pending, application no. 17/239,436

Portions of this text will be submitted to IEEE Transactions on Ultrasonics, Ferroelectrics, and Frequency Control (UFFT).

### 3.1 Introduction

Inspection of underwater structures such as ship hulls, bridge supports, and dams requires an underwater inspector, either human or robotic. Both man and machine have their inspection abilities significantly impaired in cloudy, turbid water as the suspended particles occlude visual inspection. Additional light does not solve the problem, as the light simply reflects off the particulates, just as toggling high beams on a car do not make driving through fog easier. The United States Navy recognized this challenge and began developing a heads-up display integrated into a diving helmet that could interface with a surface-mounted 3D sonar imaging device [2]. While a remotely located imaging device can improve a diver's spatial awareness, an imaging device on the diver's person to map the immediate work area with high resolution would lead to significantly more natural interactions with the environment.

Modern sensors and algorithms can create 3D maps of their surroundings for localization and path-planning for both road-based autonomous vehicles [19] and indoor rooms [20]. However, these systems are not suitable for zero-visibility underwater conditions because water attenuates microwaves (radar), radio waves (GPS, Bluetooth, WLAN, etc.), and the suspended particles block light, both visible (stereo cameras) and near-visible (lidar). As such, acoustic imaging alongside inertial and dead reckoning sensors are the standard for Autonomous Undersea Vehicle (AUV) navigation [21]. Low-frequency Sonar ($<$ 100s kHz) has seen widespread use in long-range undersea imaging, albeit with relatively low resolution. Higher frequencies, broadly called ultrasound, produce higher resolution images in the near field. Ultrasound imaging (1-15 MHz) is frequently used in medicine for non-invasive inspection of internal bodily structures through an opaque medium and shows promise for high resolution acoustic imaging in turbid water.

Several short-range sonars operating with ultrasound frequencies exist on the market. The Dual Frequency Identification Sonar (DIDSON) (Sound Metrics Corp, WA, USA) operates at either 1.0 MHz or 1.8 MHz at a range of 1m to 40m. The beam angle of 0.3°in 1.8MHz mode corresponds to a 5.2mm resolution at its minimum range of 1m [22]. An updated device, Adaptive Resolution Imaging Sonar (ARIS) (Sound Metrics Corp, WA, USA), operates at 1.8 MHz or 3.0 MHz at a range of 5m-40m and 1m-15m respectively. The

high frequency mode has an improved beam angle of 0.2°, corresponding to a 3.5mm resolution at 1m [23]. Both devices have seen use in ship hull inspection [24], imaging schools of fish for automated migration counting [25] and fish length measurement for fisheries [23]. Both devices have minimum working distances of greater than 1 meter, which is beyond the reach of a diver's arm. Additionally, their bulk requires that the diver hold the camera, further limiting dexterity while working.

This work is toward a proposed sonar sensor able to resolve structures under 3.0 mm in size at distances within arm's reach for a diver. Specifically, this work aims to focus the vertical component of the ultrasound beam using a series of curved acoustic mirrors. Acoustic mirrors have been used to collect and reflect acoustic "daylight" onto a 2D hydrophone array to produce a low-resolution image of undersea targets [26] and for focusing ultrasound pulses originating from laser bursts for Photoacoustic Microscopy [27]. Recent work has demonstrated the use of a fast-moving reflector in a clinical setting to create a 3D scan using a 1D transducer without translating [28]. This device does not modify the beam shape from the transducer, so elevational focus is comparable to the ultrasound source.

This work develops a device that uses acoustic mirrors to both shape and scan the beam concurrently in order to produce sharp images at depths much further than traditional ultrasound probes.

### 3.2 Acoustic Imaging Principles

An acoustic image is a reproduction of objects in space based on the reflections of acoustic energy. The most common method of acoustic imaging is medical ultrasound in which a probe emits a sound pulse higher than human hearing and listens for reflections. Figure 3.1 shows the working principle of using sound for imaging. As an acoustic pulse hits the interface between two different materials, the wave is partially reflected and partially transmitted. The ratio of reflection to transmission depends on the Reflection Coefficient:

$$R = \left(\frac{Z_1 - Z_2}{Z_1 + Z_2}\right)^2 \tag{3.1}$$

$$Z = v\rho \tag{3.2}$$

where Z is the Acoustic Impedance, which is the product of the material sound velocity, $v$, and density $\rho$ [29]. Note that if impedances are similar, less energy is reflected than transmitted. Since the proposed sonar device will be mapping metal or stone surfaces in a water medium, the impedance mismatch is expected to be high, thus reflecting most of the energy rather than transmitting it. As such, the system is unlikely to receive second reflections like those in Fig. 3.1, so it will likely map only the first surfaces.

The depth of a reflecting object can be found based on the speed of sound in the medium and time between the transmitted pulse and the received reflection. The first ultrasound equipment operated using a single beam

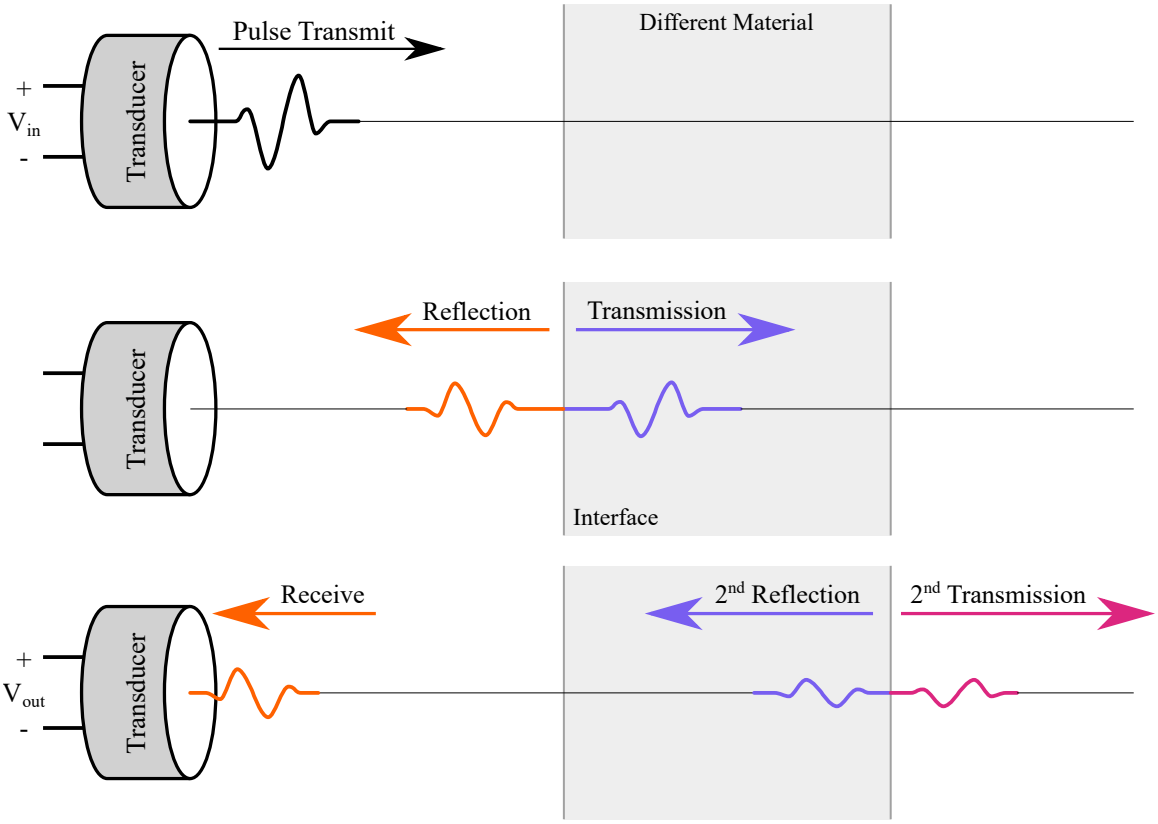


Figure 3.1: Fundamentals of Acoustic Imaging.

and receiver and acted as a rangefinder along a single axis, known as A-mode. Sweeping multiple A-mode beams in a plane results in a tomographic image, i.e. a slice of the 3D environment. This differs from typical optical images which are projections of a 3D environment on a 2D sensor plane. Note that most B-mode images are taken with an 1D array of transducers rather than sweeping a single transducer.

### 3.2.1 Pressure Field Equations

The acoustic pressure field is the pressure amplitude gain compared to the pressure source signal for any point of interest. Fig. 3.2 shows that a pressure point source produces a circular wave front that radiates outward. Arranging multiple point sources on a single line approximates a transducer aperture. The circular wave fronts superimpose on each other in area directly in front of the aperture, resulting in a beam of relatively high pressure that propagates though the medium.

The analytical formulation for pressure field is dependent on the aperture distribution function, $A(x,y)$, which describes the physical configuration of the pressure source. For a uniform aperture, the aperture distribution function is 1 where a pressure source exists and 0 otherwise. It can also act as a location-dependent pressure scaling term if pressure is not uniform over the aperture. If the function can be expressed

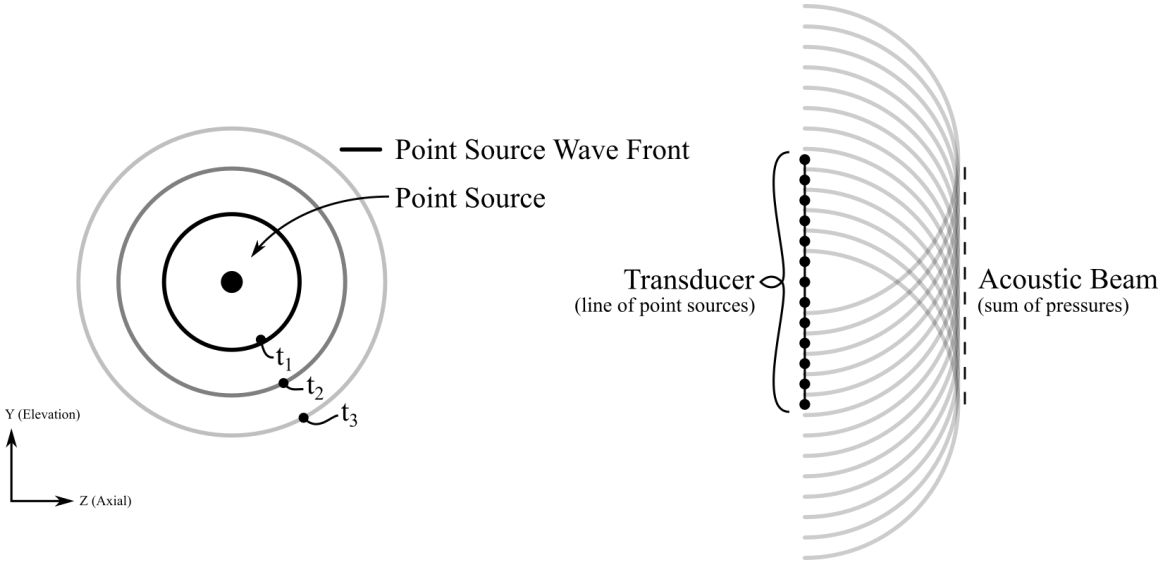


Figure 3.2: Radiation patterns of a point source and an array of point sources arranged into a rectangular aperture.

as separate functions for x and y directions, i.e. $A(x,y) = A_x(x)A_y(y)$, then the pressure field can be separated into x and y components for independent analysis [30]. Since a uniform, rectangular aperture of dimensions $L_x, L_y$ can be described as

$$A(x,y) = rect(x/L_x)\, rect(y/L_y) \tag{3.3}$$

$$rect(r) = \begin{cases} 1, & if\ |r| \leq 1 \\ 0, & otherwise \end{cases} \tag{3.4}$$

azimuthal (XZ plane) and elevational (YZ plane) focusing can be designed independently. Therefore, the proposed device will use fixed focus mirrors for the elevation direction and rely on electronic beamforming if azimuth focusing is required. A transducer's lateral resolution is the smallest distance in a plane parallel to the aperture plane distinguishable between two structures [31]. This is often measured as the -6 dB beamwidth at the imaging depth in question, and based on the far field pressure field analytical solution [30],

$$resolution_{lateral} \propto \frac{\lambda z}{D} \tag{3.5}$$

where $\lambda$ is the imaging wavelength, $z$ is the imaging depth, and $D$ is the width of the imaging aperture. Axial resolution, the distinguishable distance between two structures parallel to the axis of beam propagation is half the spatial pulse length, meaning

$$resolution_{axial} \propto \zeta\lambda \tag{3.6}$$

where $\zeta$ is the transducer damping and $\lambda$ is imaging wavelength [32]. Higher damping causes fewer element oscillations, resulting in a pulse with a smaller overall spatial length. Note that resolution is measured as a distance, so a "high resolution" system counterintuitively seeks to minimize resolution. Improving both lateral and axial resolution by decreasing $\lambda$ comes at the cost of penetration depth as attenuation in water increases exponentially with decreasing $\lambda$. The wave attenuation in water for a 4MHz signal is 0.0347 dB/cm, meaning that the signal will attenuate 7dB due to transit through the medium alone for a target at 1m [29]. Mitigating this trade-off through hardware design is one of this work's goals.

### 3.2.2 Focusing

The purpose of focusing the transmitted signal is to maximize the amount of energy directed to the area of interest, thus maximizing the energy reflected, and increasing the received signal amplitude. Focusing also prevents reflections from unwanted locations by insonifying a smaller area, allowing the transducer to differentiate between smaller "reflective" and "non-reflective" surfaces.

Focusing occurs when the phases along a plane wave are modified to match a transducer where each pressure source is equidistant from the focal point, *i.e.*, arranged on a circle. Fig. 3.3 illustrates that the wave fronts for each point source superimpose to form a circular wave front with the same center of curvature as the circular transducer. As the beam wave front progresses, it concentrates to the focal point, resulting in maximum pressure and minimum beam width.

Different focusing methods attempt to modify the beam phase to match that generated by the circular aperture [31]. Beam Forming, or electronic focusing, adjusts the phase of individual elements during transmit. Note that this requires that each point source on the transducer be commanded individually, making it only possible in directions that have multiple elements. The transducer in this system has multiple elements in the azimuth direction, but only one element vertically. Acoustic lenses made from materials with a different sound speed to water can speed up portions of the wave, resulting in an effective phase shift. Note that the lens must match the impedance of the medium or face efficiency loss due to reflections. Finally, a curved acoustic mirror changes the beam's phase by modifying the beam traversal distance. Forcing some sections of the beam travel longer than others results in a location-dependent phase shift. Note that focusing also works in the opposite direction; a point target scatters a circular wave front whose phase should be modified such that the entire aperture is excited by a beam of the same phase in order to maximize receive signal.

## 3.3 Mechanical Design

The sensor hardware has three main design goals, 1) sweep the beam in the elevational direction to collect multiple tomographic images, 2) perform elevational focusing for sharp imaging between 0m and 1m, and 3)

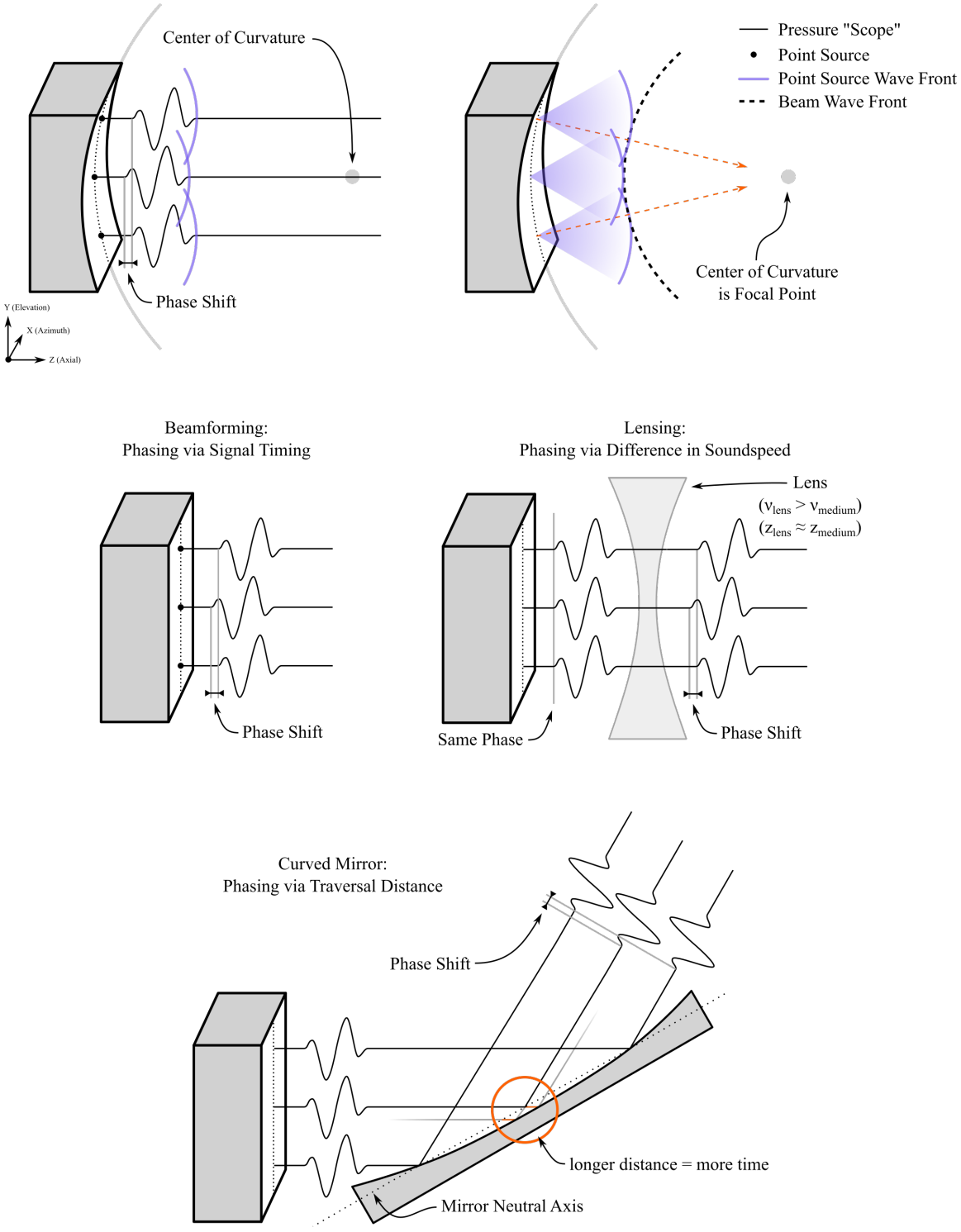


Figure 3.3: Radiation patterns of a point source and an array of point sources.

mount to a diver's body for hands-free operation.

A schematic of the sensor hardware can be found in Figure 3.4. The system is based around a custom curvilinear ultrasound transducer (Sonic Concepts, Bothell, WA, USA) with a center frequency of 4.2MHz. The 1x128 element array has an 11mm elevational aperture and is curved about the elevational axis with a 40mm radius and 50° horizontal aperture. The focusing system design consists of three acoustic mirrors, two stationary and one articulating for vertical scanning. Mirrors were chosen over lenses for the promise of large apertures with comparatively shallow depth requirements.

The mirrors' radii and locations were designed to minimize elevational beam spread at a vertical surface 50 cm from the transducer using ray-tracing in OpticStudio (Zemax LLC, Kirkland, WA, USA). Figure 3.5 shows the design results for three positions of the curved scanning mirror, demonstrating a 24° elevational field of view. Each active mirror surface is cylindrical with the YZ cross section defined by the OpticStudio design.

The scanning mirror shown in Figure 3.4 is a single-sided curved reflector designed to "wobble" about its axis in order to scan. This design was chosen for this first prototype for its ease of fabrication and simplicity in non-motorized tests. It is, however, just one solution of many possible geometries that match the mirror locations and curvatures in Figure 3.5. A recommended path for future iterations is to design the scanning mirror with a multi-sided polygon cross section with curved mirror surfaces on each side. Such a design would do away with continual acceleration and deceleration of the mirror and allow continuous rotation. This should result in less vibration and faster scan updates.

Every critical mating surface on the housing, mirrors, and bearing locators is designed to be CNC milled in the same setup to minimize chances for misalignment. While modularity is not an explicit goal of this device, it is a favorable side-effect. The majority of parts can be retained though significant modifications mirror curvatures ($\pm$100s of mm) and slight modifications to locations ($\pm$10s of mm).

### 3.4 Hardware Measurement and Results

A block diagram and a photograph of the physical hardware validation setup are found in Figures 3.6 and 3.7 respectively. The transducer is driven by a Verasonics Vantage 128 (Kirkland, WA, USA) with an unfocused plane wave upon a timing trigger signal. The transducer and it's focusing hardware is bolted to guide rails retrofitted on a 275 gallon, 40"x48"x46" tank filled with water. A custom designed 2DOF stage moves a hydrophone to programmed points within its approximately 1m x 1m range of motion. Both the guide rails and the 2D stage can be adjusted to move the hydrophone measurement plane to different depths from the hardware. A microcontroller is used to control both the hydrophone position and the triggering for the whole system. Prior to each run, it is programmed with the desired points for data collection. During the run, it

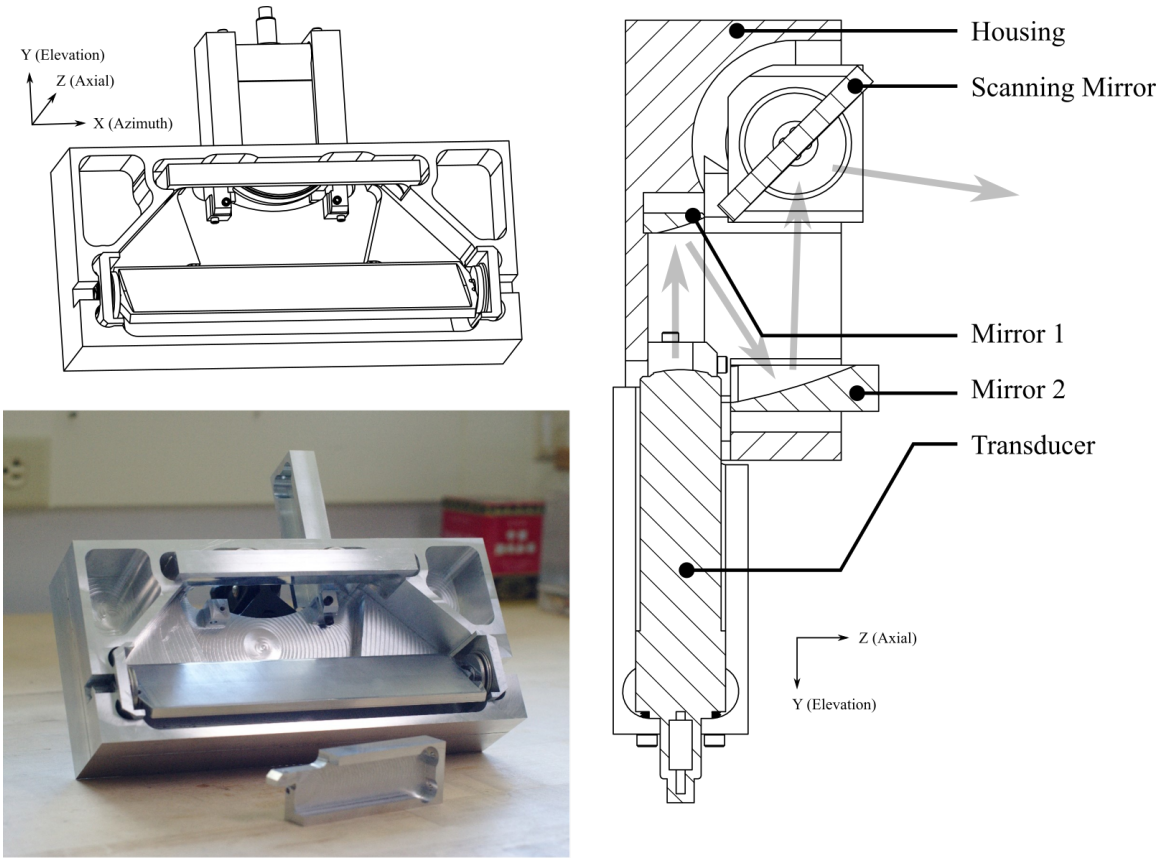


Figure 3.4: Schematic and photograph of the focusing hardware. The grey arrows indicate the beam's path through the device.

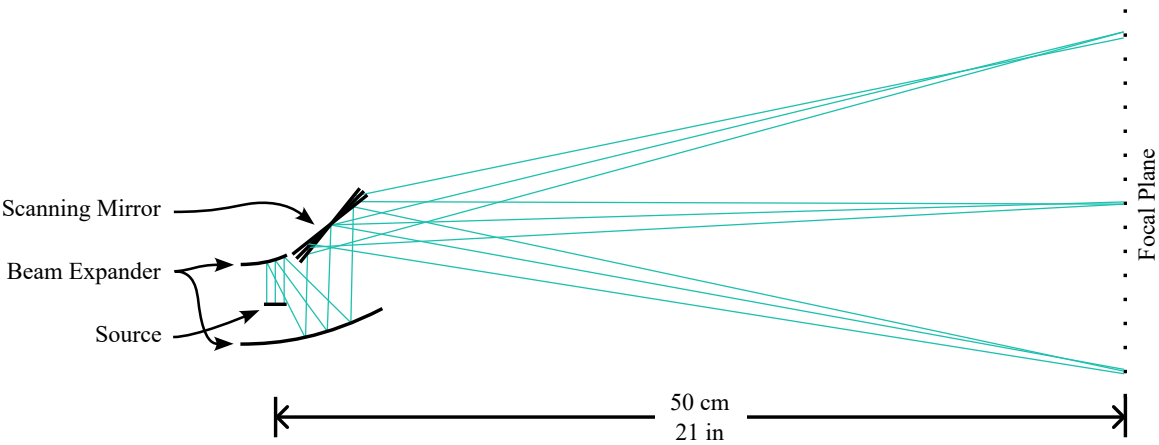


Figure 3.5: Mirror geometry as designed using ray-tracing software

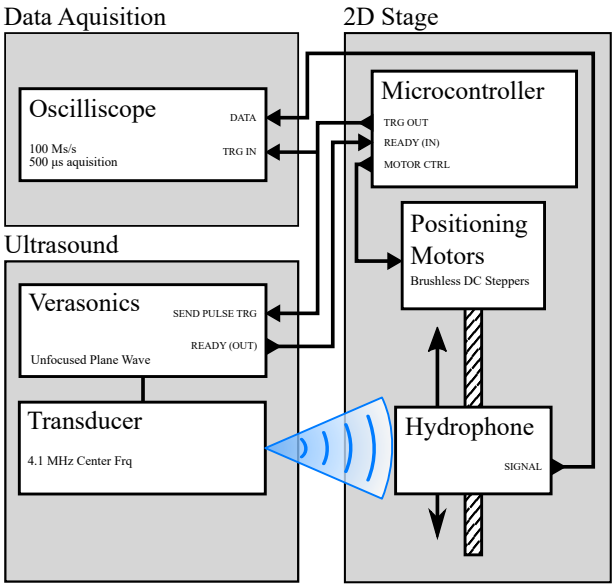


Figure 3.6: Block Diagram of the physical hardware validation, including the 2D stage controls, data acquisition, and ultrasound driver.

commands the 2D stage to move to the desired position, waits for the motion to settle, and sends a signal pulse to trigger both the ultrasound pulse and the data acquisition system simultaneously. When triggered, the data acquisition system takes 500 µs (greater than transit time across the tank) of voltage data from the hydrophone at 100 Ms/s, which is more than 12x the Nyquist frequency for a 4MHz signal. Data collection is repeated 6 times at each location to allow for averaging during post-processing.

Pressure waves were measured over planes parallel to the XY plane for several Z depths which were then used to calculate the acoustic intensity $I$.

$$\Delta P = \frac{max(P) - min(P)}{2} \tag{3.7}$$

$$I = \frac{(\Delta P)^2}{2\rho v} \tag{3.8}$$

$$I_{dB} = 10 * log_{10}\left(\frac{I}{I_{max}}\right) \tag{3.9}$$

where $\rho$ is the density of the medium and $v$ is the speed of sound in the medium. The intensities for multiple planes can be averaged across identical Y points and plotted as a function of Z to visualize how the beam focuses and expands as it transits through the medium. An example of the resulting acoustic intensity field on the YZ plane can be seen in Figure 3.8.

As described in Section 3.2.2, the -6dB beamwidth is the standard measure of lateral resolution for an ultrasound system. This beamwidth is calculated by normalizing the acoustic intensity at the maximum

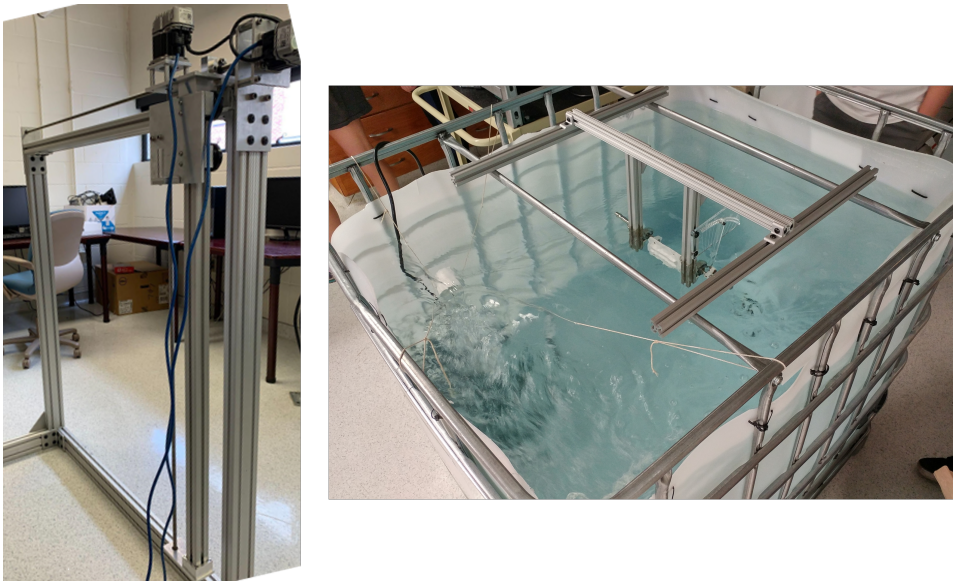

Figure 3.7: Photographs of of the hardware validation test setup. The 2D stage is shown to the left and the 275-gallon testing tank is on the right.

| Mirror Angle $\theta$ | Minimum Beamwidth | Depth |
|---|---|---|
| +0° | 7.3 mm | 0.40 m |
| +6° | 8.6 mm | 0.40 m |

Table 3.1: Minimum -6dB beamwidth (elevational resolution) measured on the hardware.

intensity for each depth, then finding the distance between the -6dB intensities. The measured beamwidths, and therefore elevational resolution, for the hardware are listed in Table 3.1.

The discrepancy between the desired 3.0 mm resolution and the measured resolutions is likely due to two simplifying assumptions during the ray-tracing design phase. The first is the assumption that the acoustic source acts like a collimated laser. In reality, there are diffraction effects in the transducer's near field that may negatively affect how the acoustic mirrors reflect the beam. The second is that the transducer has a protective lens with a focus at infinity. All transducers typically have a silicone-like material in front of the piezoelectric elements to both protect the fragile crystals and to provide focusing for its intended application. While the focus of the custom transducer was requested to be infinity, the manufacturer warned that there may be a focal point due to manufacturing constraints. Both of these effects would be difficult to impossible to design around using the ray-tracing method, and instead require a more sophisticated model like that described in the next section.

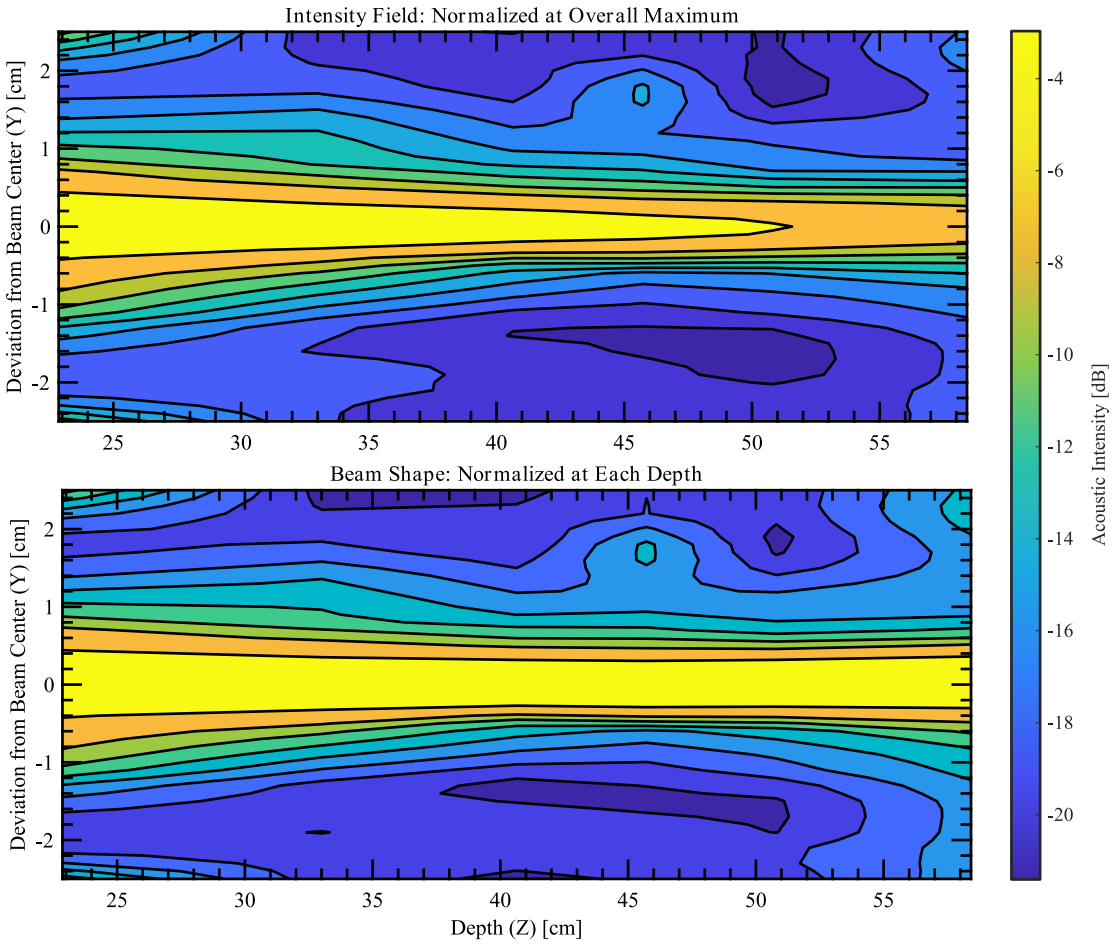


Figure 3.8: Plots of acoustic intensity field and the beam shape for $\theta = +6°$ as measured on the hardware.

### 3.5 Simulation Model

An acoustic simulation of the system was built to model how the ultrasound beam interacts with the acoustic mirrors in order to calculate the acoustic intensity fields for arbitrary scan angles. This allows for the calculation of the acoustic field and can be used to test future iterations to mirror geometry before fabricating a new device. The simulation can be broken into sub-components as shown in Figure 3.9: A) beam expander interactions, B) propagation from the curved mirror to the rotating scanning mirror, and C) calculating pressures at points in the far field.

Sub-component A was built in k-Wave (www.k-wave.org), an open-source toolbox for MATLAB designed to model the time-varying acoustic field for user defined sources and mediums. Rather than a typical finite-element model that solves for the deformation of a medium, k-Wave uses a solution to the wave equation that uses the inverse Fourier transform to calculate spatial pressure gradients, which is more computationally efficient [33]. This simulation is configured with a pressure source matching the size and location of the

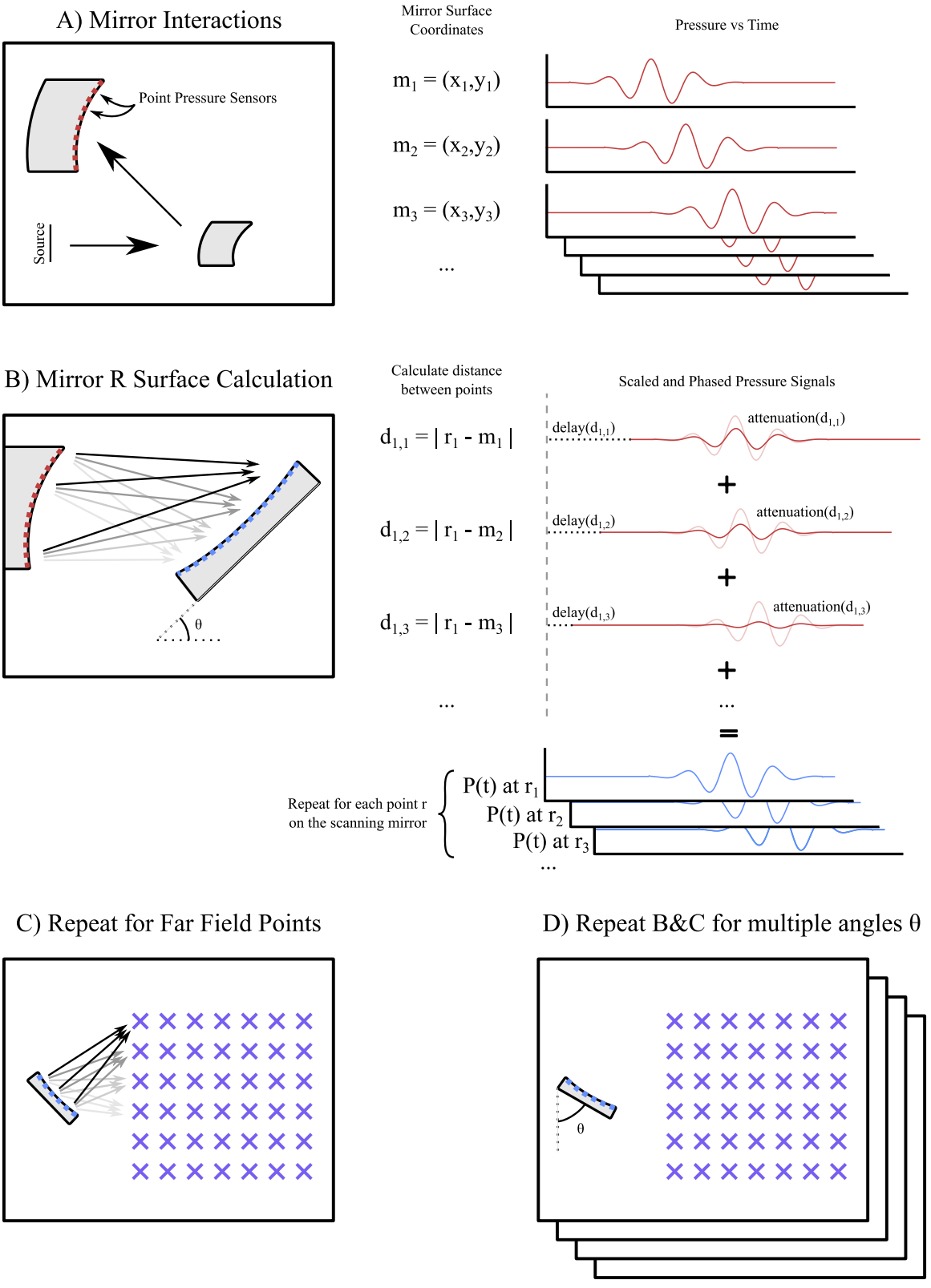


Figure 3.9: Acoustic simulation overview.

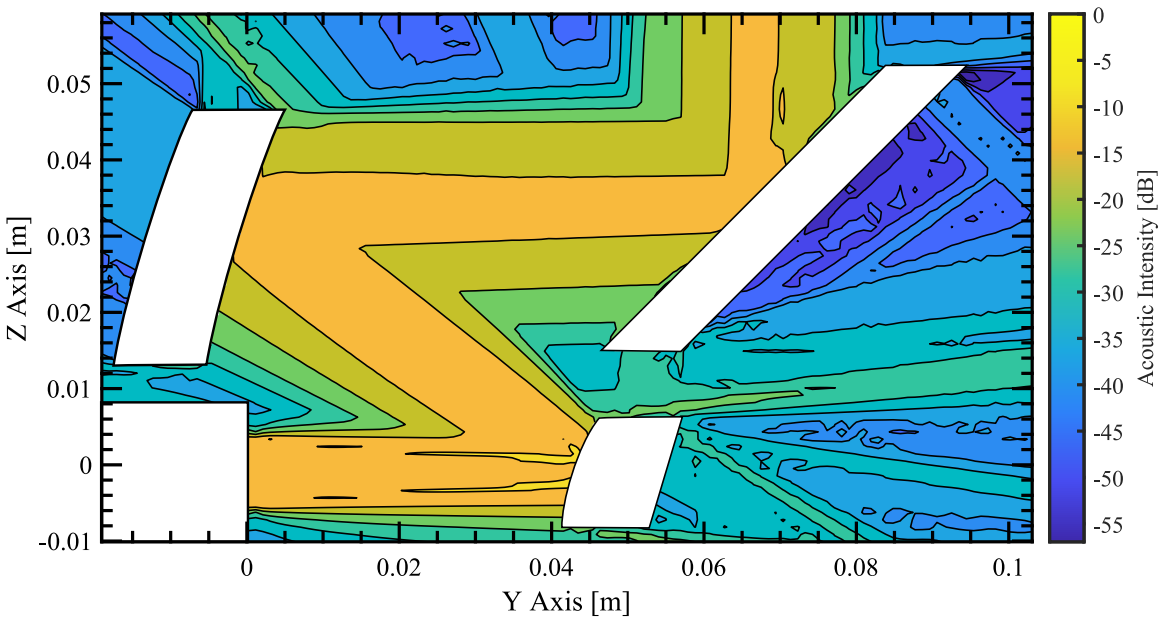


Figure 3.10: Simulated acoustic field between mirrors shows the path and amplitude of the acoustic beam.

ultrasound transducer in the design in Figure 3.4. The pressure source waveform is a 3 MHz Gaussian Pulse with a fractional bandwidth of 0.6. Note that no effort was made to match the hardware's and the simulation's pressure magnitudes as acoustic intensity is typically measured in dB, which is a unit measured relative to a maximum. Next, the simulation medium's density and sound speed was modified in the mirror regions as defined by their designed geometry. This allows k-wave to simulate the acoustic reflections from the aluminum mirrors. Finally, k-wave was configured to output the time-domain pressure signal for each simulation grid point on the surface of the second stationary mirror and in a coarse grid. The mirror surface data is used in later simulations, where the grid data can be used to visualize the beam's interaction with the mirrors as seen in Figure 3.10.

The simulation method of sub-components B and C are based on the propagation of point sources through a medium as explained in Section 3.2. The pressure waveform at a distance $d$ from a point source is an attenuated and phased version of the original point source waveform depending on $d$. A reflecting surface can be modeled as a collection of point sources, therefore the pressure at a remote point is proportional to the sum of each point source with an attenuation and phase.

$$attenuation(d) \propto \frac{1}{\sqrt{d}} \tag{3.10}$$

$$delay(d) = \frac{d}{c} \tag{3.11}$$

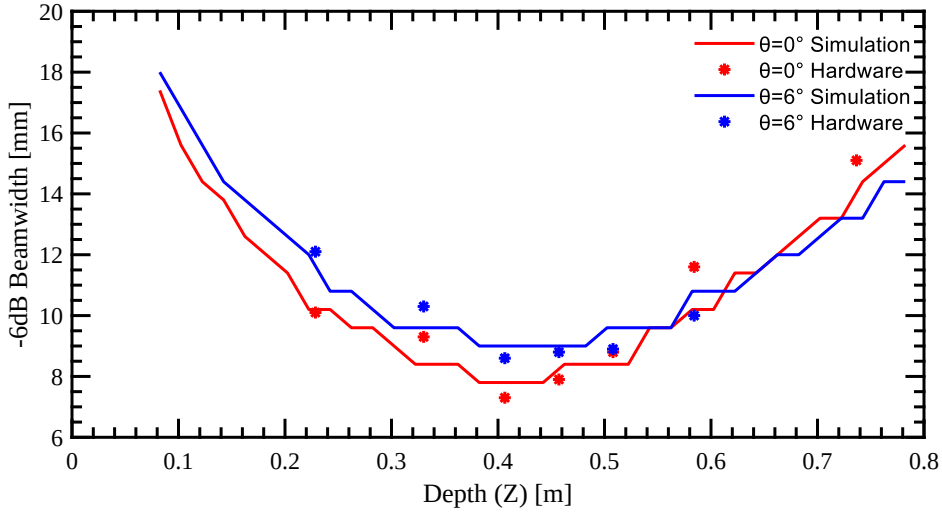


Figure 3.11: Calculated -6dB beamwidth for both simulation and hardware measurement.

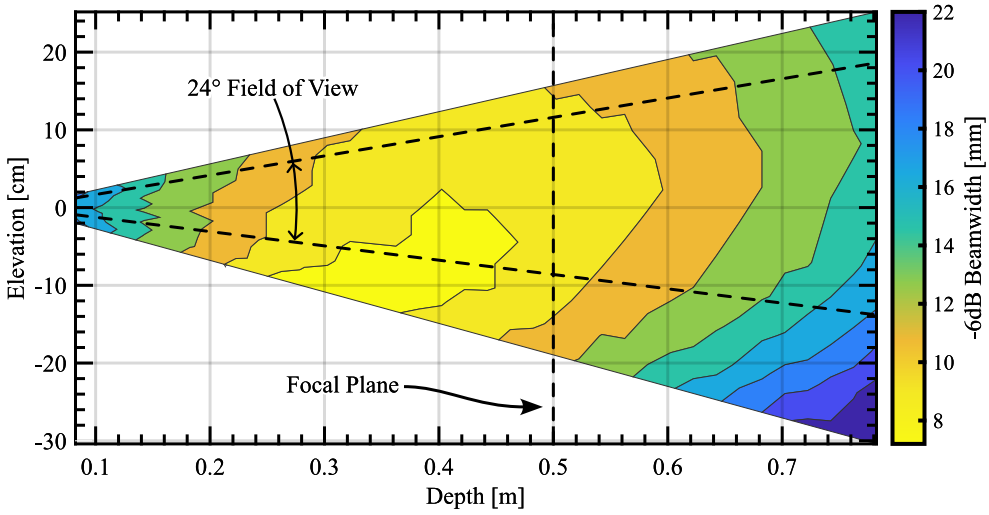


Figure 3.12: Simulated elevational resolution for $\pm 10°$ swept field of view.

$$P1 \propto \sum_{n} attenuation(d)\, P0_n\,(t - delay(d)) \tag{3.12}$$

This method is used to calculate the pressure waveforms at each point on the rotating mirror surface using the beam expander mirror as the source, then calculate the pressure waveforms at far field points using the rotating mirror surface as the source. With the far-field pressures calculated, the acoustic intensity field can be calculated identically to the hardware measurements using Equation 3.9. Figure 3.11 shows good agreement between the -6dB beamwidth calculated using measurements from hardware and simulation, suggesting that this model accurately describes the physics of the focusing system.

Sub-components B and C are then repeated for multiple angles of the rotating mirror, $\theta$, to simulate a scan. The beamwidth vs depth at each angle can be assembled into a spatial visualization of device resolution. Figure 3.12 is a visualization of the expected vertical resolution of the device across the scanned area. Both Figures 3.11 and 3.12 show that the device's vertical resolution changes with respect to both depth $Z$ and scanning mirror location $\theta$. This means that the device will have a "sweet spot" where the resolution is higher than the surrounding areas, thus, a region of sharper details. Since this device is intended to be positioned by a human with real-time visual feedback, the operator will naturally gravitate to positioning their work area within the highest resolution area, just as those with insufficient glasses will move their work to somewhere they can see sharply.

The resolution is fairly uniform between 25 cm and 55 cm (approx. 1 - 2 ft), which is an excellent viewing range for a diver manipulating objects with their hands. Although the resolution is roughly 50% worse at a depth of 80 cm (approx. 3 ft) than the optimal working area, this is still sufficient to give a diver some far-sightedness to navigate their immediate surroundings and to close in on a target. This plot can be used to optimize the mirror geometry to improve not only peak resolution, but also resolution uniformity within the working region.

### 3.6 Conclusion

This work proved the viability of a high-frequency sonar device for visualizing solid objects underwater using ultrasound in a field-of-view and range useful to a human diver. This work proposed a novel design to use acoustic mirrors to focus and scan the ultrasound imaging direction over a 24° field of view and validated its performance using fabricated hardware and an acoustic simulation. While the specific design fell short of the targeted 3.0 mm vertical resolution, the device shows promise in its ability to 1) focus an ultrasound beam an order of magnitude further away than typical medical ultrasound, and 2) use an acoustic mirror to scan the beam across a three dimensional area. Finally, this work lays the groundwork for future refinements thanks to building a flexible acoustic simulation and validating its results against hardware.

### 3.7 Future Directions

This work laid the exploratory groundwork for more refined future iterations of this device. The simulation of the beam expander suggests that the first two mirror surfaces may be too small to sufficiently capture the expanded beam. Larger mirrors would result in a functionally larger aperture, and therefore, a better elevational resolution. Additional refinements to the mirror locations and curvatures can be made using the full acoustic simulation.

Designing a series of flexible acoustic mirrors using either thin gauge sheet metal or machined flexure

features could allow for the focal plane to be adjusted by the operator in real time. This would allow the device to have a long-range mode for navigation to a worksite and short-range mode for working within arms' reach. The wavelength of a 4 MHz acoustic signal in water is 0.37 mm (0.015 in). Flexure features should be smaller than $1/15^{th}$ of the wavelength, resulting in a target of approximately 0.001 in. Such precision is possible with conventional machining.

# CHAPTER 4

## Mock Circulatory Loop

Portions of this text previously appeared in:

**J. Howard**, S. Thomas, C. Gallentine, and E. Barth, "Hydraulic Test Stand to Model Circulatory System Dynamics for Artificial Heart Evaluation," in BATH/ASME 2021 Symposium on Fluid Power and Motion Control, 2021.

Portions of this text will be submitted to the American Society for Artificial Internal Organs (ASAIO) Journal.

### 4.1 Introduction

For people living with advanced heart disease, cardiac transplant is often the treatment of choice when all other options have been exhausted. For some, mechanical circulatory support (MCS) devices, including ventricular assistive devices (VADs) and total artificial hearts (TAHs), are a bridge to transplant, while for others for whom surgery isn't an option (for lack of available donor hearts or other complications), these devices are often a destination therapy [6]. State-of-the-art VAD and TAH technologies have led thousands of patients to better clinical outcomes and higher qualities of life, but they are not without risks and drawbacks.

Long-term, many patients implanted with MCS devices require further monitoring and treatment due to the circulatory system's exposure to high-shear, non-pulsatile flow [34]. Such flow, often from compact and efficient continuous-flow VADs, is associated with increased chances for blood infections, stroke, hemolysis, and platelet activation [35], and the need for possible reoperation [36]. Recipients are also exposed to increased risk of thromboembolic events [37], aortic insufficiency [38], and gastrointestinal bleeding [39,40].

Recently, researchers have proposed novel, compact pump designs using principles from industrial fluid-power technology to retain the size and durability advantages of continuous-flow VADs while adding low shear, pulsatile flow capabilities. Candidate designs include rotary piston pumps [41], spherical gerotors [42], and sliding vane pumps [43].

To further these emerging technologies, prototypes must be evaluated against a load that closely resembles the human circulatory system. This work examines the design of a mock circulation loop (MCL) engineered to approximate the cardiovascular system's characteristic resistance, capacitance, and inertance, following established Windkessel modeling principles. An MCL that is representative of the dynamic loads of the cardiovascular system will enable control design of TAH and VAD prototypes. As will be seen, a first principles based modeling approach using bond graphs provides immediate insights regarding either flow or pressure

control of such a prototype. The authors begin with an outline of various Windkessel configurations and their modeling implications, concluding with a review of representative Windkessel estimates for human cardiovascular resistance, capacitance, and inertance. These lumped parameter estimates along with the predicted performance of the authors' proposed hardware are simulated against reference cardiovascular pressure and flow data. Hardware selection is then outlined against governing physical equations to conform the loop to the Windkessel estimates as closely as possible.

## 4.2 Review of Windkessel Models

Prior to a heartbeat, the left ventricle fills with freshly oxygenated blood from the lungs in the diastolic phase. Then the heart beats, forcing the left ventricle to empty its contents into the aorta. This charge of oxygenated blood causes the aorta to inflate like a balloon partially to store the new volume of blood. Although blood is not actively pumped during the diastolic phase, the aorta's storage ability smooths out the pulsatile pumping action of the heart and provides a continuous supply for the arteries.

The Windkessel model aims to mathematically describe this effect in order to estimate aortic pressure given a cardiac flow rate, or vice versa. Otto Frank popularized this model in a 1899 paper presenting the mathematical equations to estimate cardiac output though pressure [44]. The Windkessel (a German word meaning "Air Chamber") was a device equipped on fire trucks to smooth out the pulsatile flow of hand pumps to ensure more constant flow to the firefighter's hose, analogous to how the aorta's elasticity smooths the cardiac output [45]. In recent decades, the Windkessel model has come to label any lumped parameter model that includes aortic or arterial compliance in its definition of dynamic impedance.

### 4.2.1 Two-Element Windkessel

The simplest Windkessel model uses two elements, an elastic reservoir to model aortic elasticity $C$ and a flow restriction to model the peripheral resistance $R_p$ of the arteries and capillaries. This model's parameters are estimated by fitting a time constant to the exponential decay of the arterial pressure during the diastolic phase. The aortic compliance estimated using this model closely matches the aorta's material properties [44]. The model is mathematically identical to a low-pass filter, as seen in Figure 4.1. Although it accurately predicts the aortic pressure as it empties between heartbeats, predictions for systolic phase are not accurate. Despite this limitation, test stands based on this variant have been used for in vitro testing of biologically active heart valves [46].

From a dynamics standpoint, the Bond Graphs in Figure 4.1A show that the compliance element is only in integral causality for a flow source. For an effort source, the system does not have any states, and is therefore not dynamic.

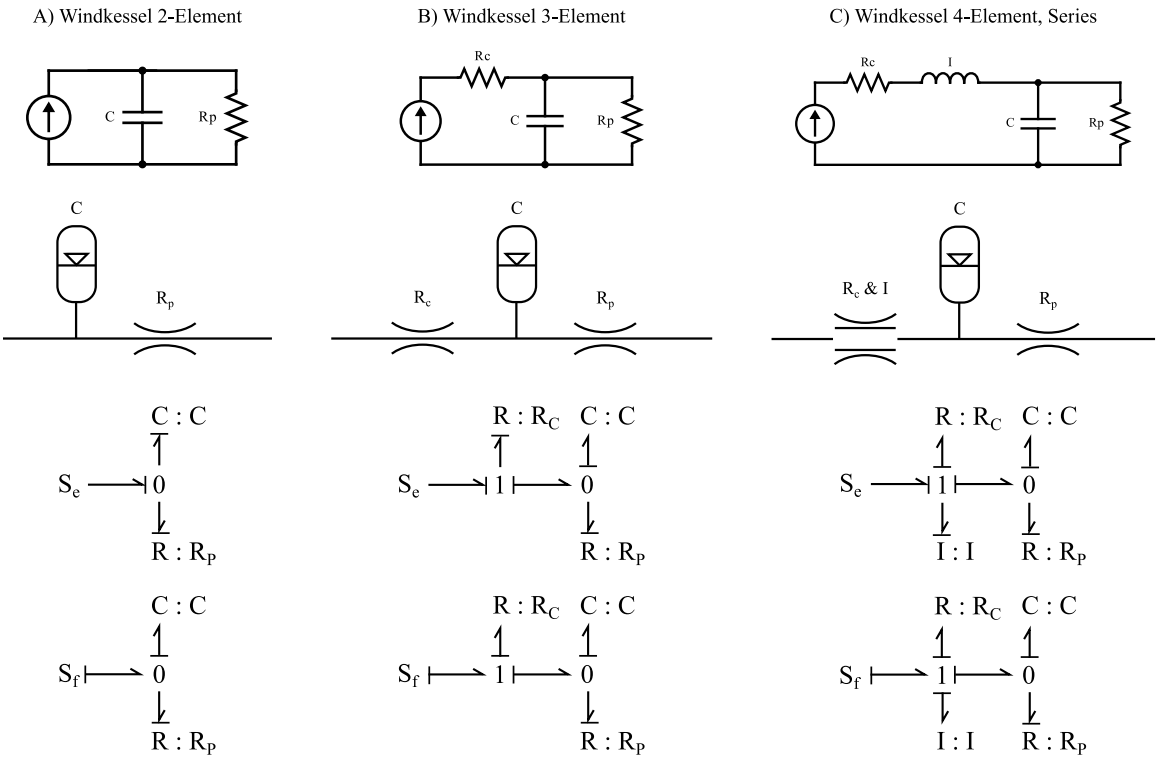


Figure 4.1: Various forms of the Windkessel model expressed with an electrical equivalence, hydraulic equivalence, and bond graph notation.

### 4.2.2 Three-Element Windkessel

The additional characteristic resistance term $R_c$ included in the 3-element model is a simplification of the aorta's hydraulic resistance and is used to improve the model prediction of aortic pressure during the systolic phase. This model can be used to demonstrate how changes in peripheral resistance can affect cardiac load. The additional system resistance causes parameter estimation to overestimate the aortic compliance compared to its material properties, and can only be used to qualitatively explain changes in blood pressure due to compliance changes [44]. *In vitro* test stands are commonly based on this variant due to its realistic and predictable impedance [47, 48].

Both Bond Graphs in Figure 4.1B show the compliance element in integral causality, therefore the system acts dynamically regardless of the input source type.

### 4.2.3 Four-Element Windkessel

The characteristic inertance element $I$ aims to further refine the systolic response by modifying the low-frequency behavior of the characteristic impedance [44] by adding kinetic energy storage. The literature is split between placing the inertance term in series, Figure 4.1C, or in parallel (not shown) with the characteristic resistance. Both are possible from a mathematical model standpoint; however, only the series model

Table 4.1: Parameters for the 4-Element Windkessel

| | $R_c$ | $I$ | $C$ | $R_p$ |
|---|---|---|---|---|
| | Pa s $m^{-3}$ | Pa $s^2$ $m^{-3}$ | $m^3$ $Pa^{-1}$ | Pa s $m^{-3}$ |
| Sharp (1999) [51] | 5.30e+6 | 3.12e+5 | 1.77e-8 | 1.25e+8 |
| Burattini (2007) [52] | 3.84e+6 | 5.00e+4 | 2.09e-8 | 1.22e+8 |
| Kung (2011) [48] | 2.45e+7 | 7.00e+5 | 2.3e-9 | 4.05e+8 |

makes sense in the hydraulic domain. Parallel elements in the hydraulic domain imply two separate flow paths: one with a restrictive pipe, and a second open path with fluid inertia effects. This model is prolific in the literature [49, 50] despite the cardiovascular system not containing two flow paths from the heart into the aorta. It is unclear what, if any, physical phenomenon exists that the parallel inertance describes. Therefore, the series model will be used as the basis for simulation and hardware design in this work.

From the Bond Graph in Figure 4.1C, a 4-element model with a flow source results in an inertance term in derivative causality, leaving only one storage element in integral causality. This system, therefore, has only one degree of freedom and is not capable of oscillation. The same 4-element model with a pressure source, however, puts both the inertance and capacitance in integral causality, making this a $2^{\text{nd}}$ order system.

### 4.3 Discussion of Lumped Parameters

Several papers have estimated parameters for the 4-element series model using clinical patient data [48, 51, 52]. These papers' results have been converted to SI units for simulation purposes and summarized in Table 4.1.

Sharp et al. (1999) mathematically modeled several lumped parameter Windkessel models, including a 2-element, 3-element, 4-element series. The data used is from a prior published work collected from five healthy men in their thirties with normal blood pressure and no signs of coronary arterial disease [53]. Sharp et al. describe the data as a representative average. The lumped parameters were found by matching the model's frequency response to the modulus and phase values calculated from the patient data.

Burattini et al. (2007) performed a very similar optimization to Sharp et al. but included more subjects. In addition to the five subjects from [53] this work also includes five subjects from [54]

Parameters estimated by Kung et al. (2011) are different from the prior two and are included to show the effects of parameter variability. That work's primary goal was to design and construct a physical Windkessel test stand to validate Computational Fluid Dynamics simulations. The data used for parameter estimation was collected from patients with abdominal aortic aneurysms and high blood pressure [55]. Therefore, simulation results from this parameter set are expected to be off-nominal. It is also worth noting that the authors of this

work did not explicitly include inertance in their design of the characteristic impedance module, nor did they estimate parameters for inertance from the data. They did, however, calculate expected inertance for their impedance module and experimentally confirm their results. As Kung *et al.* deemed the resulting model acceptable, this calculated result appears in Table 1 in lieu of a true parameter estimation.

Both Sharp and Burattini show good agreement with Peripheral Resistance estimates, and both Compliance and Characteristic Resistance are within 37% of one another. Both Sharp and Kung estimated inertance to be an order of magnitude higher than Burattini. As expected due to the non-normal patient data used, Kung estimated much higher resistances, and much lower compliance than both Sharp and Burattini, showing the dramatic physical differences that can occur patient to patient.

### 4.3.1 Implications of the Four-Element Model on Artificial Heart Design

The inertence element of the system plays a significant role in the system dynamics, and will affect the dynamics of a candidate artificial heart with pulsitile flow. The exact implications of this element depend on the class of pump and its controller.

Positive displacement pumps, such as a Gerotor or piston pump, typically move a set volume of fluid per displacement of an actuator, meaning that flow rate is determined by a positive displacement pump's speed. This class of pumps are therefore best described as flow sources. As described above, the 4-element model with a flow source puts the inertance term in derivative causality, meaning that the input pressure is determined by the time derivative of flow rate $Q$.

$$P_I = I\frac{dQ}{dt} \tag{4.1}$$

This means that a sudden change in flow rate could result in significant pressure spikes/troughs. This well-known hydraulic phenomenon is known as "water hammer" and requires intentional design to mitigate its effects. Adapting a positive displacement pump as an artificial heart should at minimum have a check valve across its input and output similar to a flyback diode on a motor controller.

Other pumps such as turbine and centrifugal pumps generate a pressure, and can be modeled as a pressure source. The bond graph shows that this configuration is a two degree of freedom dynamic system that is capable of oscillation. The resulting equation of motion is as follows:

$$\begin{bmatrix} \dot{Q_{in}} \\ \dot{P_2} \end{bmatrix} = \begin{bmatrix} -\frac{R_c}{I} & -\frac{1}{I} \\ \frac{1}{C} & -\frac{1}{R_p C} \end{bmatrix} \begin{bmatrix} Q_{in} \\ P_2 \end{bmatrix} + \begin{bmatrix} \frac{1}{I} \\ 0 \end{bmatrix} P_{in} \tag{4.2}$$

Using Sharp's parameters in Table 4.1, several insights can be made about the dynamics of the circulatory

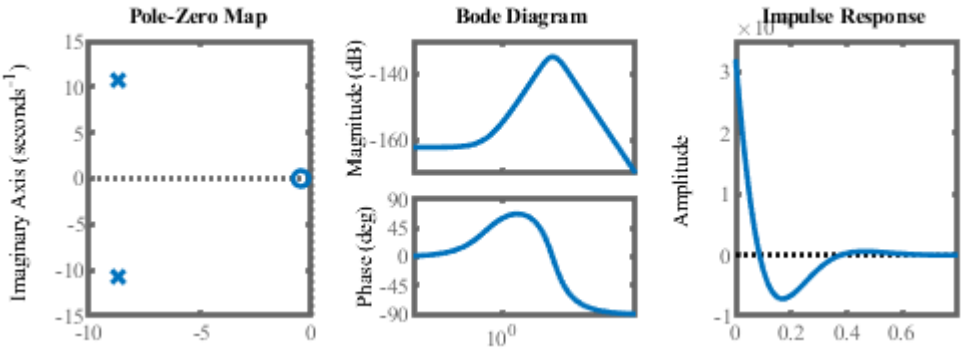


Figure 4.2: Measures of the Circulatory System Dynamics

system. The Pole-Zero plot in Figure 4.2A shows two complex poles, confirming that forcing the system with a pressure source can result in oscillatory flow rate though the heart. Interestingly, the Bode plot in Figure 4.2B shows that the circulatory system has a natural frequency centered at 2.0 Hz, or 120 BPM. Since normal heart rates range from roughly 60 BPM at rest to 180 BPM during vigorous exercise, having a natural frequency tuned at the operational midpoint means that the circulatory system will flow more blood per input pressure when excited with a normal heart rate. It should come as no surprise that the the human circulatory system is tuned to be most efficient at normal heart rates, but the result came as a welcome sign that both the model and the parameters make sense. This analysis further illustrates the importance of the inertence term in the Windkessel model: the 2- and 3-element models are 1$^{st}$ order systems, meaning that they are incapable of having a natural frequency.

### 4.4 Simulation Results

The 4-element series Windkessel modeled in Figure 4.1 was simulated using a pressure input based on aortic pressure data from an actual beating heart [54]. The simulation was repeated with each parameter set in Table 4.2 and the parameters measured for the hardware proposed in Section 4.5. The resulting flow rate predictions from the models were compared to the actual flow data from the same source in Figure 4.3.

It is important to note that the pressure and flow data used is from a single patient. Since specific parameters, especially Peripheral Resistance, can vary person to person, the “Reference” signal is for comparison only, and should not be considered a “target”.

The red, yellow, and purple lines in Figure 4.3C show simulated flow output for a patient’s aoritc pressure waveform for each parameter set in the literature. Kung’s parameters, based on patients with high blood pressure, predict significantly smaller flows when driven with a normal pressure. This makes sense as high blood pressure is not the cause, but the symptom of a more restrictive circulatory system. Indeed, Kung

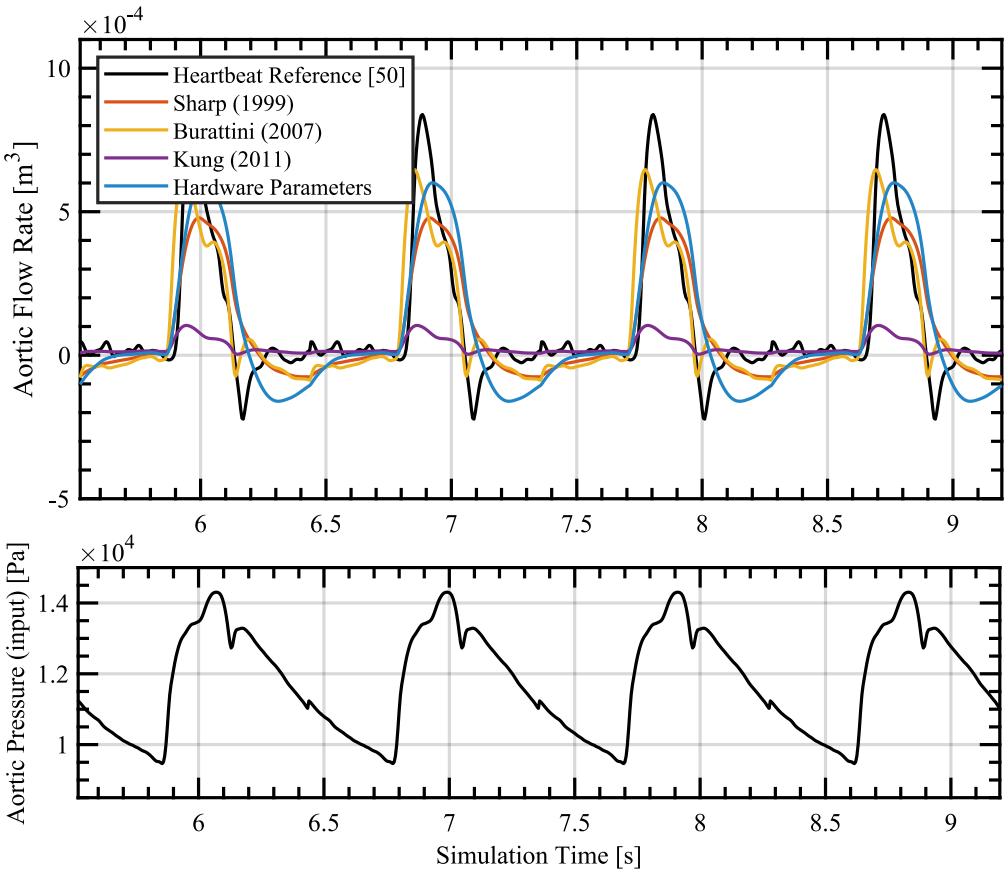


Figure 4.3: Flow prediction results for a 4-Element Windkessel model comparing different parameter sets.

estimates a Peripheral Resistance four times higher than the other estimates while Characteristic Resistance, Inertance, and Compliance parameters are within the same variance of the other estimates. The body needs the same flow rate of blood regardless of health, thus heart needs to work harder to to deliver said flow rate in patients with a more restrictive circulatory system.

Since Sharp's and Burattini's Compliance and Peripheral Resistance parameters are similar, their simulated flow rates share a similar overall shape. Though neither match the heartbeat reference data perfectly, recall that the reference is for a single patient, and patient-to-patient variability means the closeness to actual response should not be given much credence. The notable difference between the two parameter sets is changes in the "attack": Burattini's estimates result in a steeper initial slope and faster rise time than Sharp's. This is due to Burattini's estimate being 83% smaller compared to Sharp's. With less mass to accelerate in the model, Burattini's parameters react faster. Using Equation 4.35 in Section 4.5.4, one can estimate that Burattini's inertance parameter corresponds to a 0.53 in long 3/4 in diameter pipe, where Sharp's corresponds to a more anatomically realistic 3.50 in long 3/4 in diameter pipe.

| Module | Parameters |
|---|---|
| Characteristic Resistance $R_c$ | 7x 7/32" diameter holes, negligible length (thru sheet metal) |
| Inertance $I$ | 4" long, 3/4" diameter pipe |
| Compliance $C$ | 2.5" diameter piston, 3.238 lb/in spring rate |
| Peripheral Resistance $R_p$ | 1249x 1/64" diameter holes, 0.766" length |

Table 4.2: Dimensions for each Mock Circulatory Loop module

Finally, the Sharp, Burattini, and hardware parameter sets all predict a negative flow rate at certain points during the cardiac cycle. In addition to the patient-to-patient variability mentioned before, this behavior may be exasperated by unmodeled valve dynamics at the aorta's inlet. Since this paper aims to build a realistic arterial load extrinsic to the heart, this shortcoming is unimportant.

### 4.5 Hardware Design

Almost all physical systems can be modeled by the relationship between "efforts" and "flows". Electrical circuit dynamics are described with voltage and current, mechanical systems with force and velocity, and hydraulic systems with pressure and flow rate. Using this framework, a system can be translated into any energetic domain by using the efforts and flows from the respective domains. The same is true to implement the lumped parameter electrical equivalence models in Figure 4.1 in the hydraulic domain, but with the caveat that there are physical limitations that can make it difficult to match the expected dynamics without careful design considerations.

The hardware design proposed in this section is similar in basic layout and analysis to prior works, but with design decisions made in light of artificial heart pump development in a non-sterile engineering lab rather than as a load for a real pumping heart [47] or a Computational Fluid Dynamics validation bench [48]. The overall design goal is to maximize accessibility and interchangeability by keeping all elements of the device modular. This allows an end user to use the sizing information below to build modules for different parameter sets to test patient-to-patient variability and any array of pathological effects. The bench is unlikely to be used at steady state for long periods of time, as any design iterations must be manufactured and assembled prior to testing, and feedback control development requires frequent interruptions to apply controller gains. Therefore, any Mock Circulation Loop that requires extensive tuning and parameter identification prior to a test run is highly undesirable. This system aims to produce a reliable, accurate load with as little operator intervention as possible.

### 4.5.1 Compliance Module Design

In the modeling of energetic systems, a "compliance" is a potential energy storage element. In the hydraulic domain, the constitutive equation for a linear compliance is

$$P = \frac{1}{C}V = \frac{1}{C}\int Q \tag{4.3}$$

where $P$ is pressure, $Q$ is volumetric flow rate, $V$ is the volume of fluid stored in the element and the integral of $Q$, and $C$ is the compliance. This equation is more commonly written as the partial derivative of pressure with respect to volume.

$$\frac{\partial P}{\partial V} = \frac{1}{C} \tag{4.4}$$

This section outlines several designs for a calibrated compliance module, concluding with the final design selected for this work. While the third design in 4.5.1.3 worked best for the selected parameter set, the other designs may be better suited for other parameter sets.

#### 4.5.1.1 Air Spring Potential Field

Most sources in literature use a tank pressurized with air where the volume displaced by the fluid compresses the air results in increased pressure. This system uses the compressibility of air as the potential energy storage physics. The potential field is quantified by the Ideal Gas Law,

$$PV_{air} = nRT \tag{4.5}$$

where $P$ is pressure, $V_{air}$ is the volume of air in the compliance module, $n$ is the number of moles of air in the container, $R$ is the compressibility of air, and $T$ is the temperature of the fluid. Assuming that the compliance module is sealed to prevent air leakage and that temperature change is negligible during operation, $n$, $R$, and $T$ are constant. Thus, the module pressure for a given volume is

$$P_0V_0 = PV_{air} \tag{4.6}$$

$$P = \frac{V_{air}}{P_0V_0} \tag{4.7}$$

where $P_0$ and $V_0$ are the module's air pressure and volume at rest, i.e. at zero energy storage. The air volume is the total volume of the module less the volume of BMF stored in the compliance module.

$$V_{air} = V_0 - V_C \tag{4.8}$$

where $V_C$ is the volume of working fluid stored in the compliance module. Substituting 4.8 into 4.7 nets an equation of $P$ as a function of $V$.

$$P = \frac{P_0 V_0}{V_0 - V_C} \tag{4.9}$$

Then, according to equation 4.4,

$$\frac{1}{C} = \frac{\partial P}{\partial V_C} = \frac{P_0 V_0}{(V_0 - V_C)^2} \tag{4.10}$$

$$C(V_C) = \frac{(V_0 - V_C)^2}{P_0 V_0} \tag{4.11}$$

The resulting equation for compliance of an air-spring based accumulator depends on $V_0$, and is therefore nonlinear. The lumped parameter Windkessel model that this device tries to emulate contains only linear parameters. A module with nonlinear behavior may negatively affect the MCL's ability to replicate the target model.

Therefore, the design variables $P_0$ and $V_0$ should be chosen to keep the nonlinear effects within acceptable margins. First, the operating volume $V_{opr}$ and the ratio of extremes $b$ must be calculated using simulation results for the volume stored.

$$V_{opr} = mean(V_C(t)) \ , \ b = \frac{V_{extreme}}{V_{opr}} \tag{4.12}$$

These two quantities determine the design constraints for a given acceptable tolerance. Next, let $V_0$ be a multiple of $V_{opr}$ such that

$$V_0 = aV_{opr} \tag{4.13}$$

Note that as $a$ increases, the effect of a changing $V_C$ in equation 4.11 decreases. Thus, higher values of $a$ result in a more linear compliance. Then setting Equation 4.11 equal to the lumped parameter $C$ at $V_C = V_{opr}$ results in an expression relating $P_0$ and $a$.

$$C = C(V_{opr}) = \frac{V_{opr}(a-1)^2}{aP_0} \tag{4.14}$$

$$P_0 = \frac{(a-1)^2}{a}\frac{V_{opr}}{C} \tag{4.15}$$

This means that as $a$ increases, the required initial pressure $P_0$ also increases. To find the minimum $a$ that results in an acceptable error during operation, calculate the error at $V_C = V_{extreme}$.

$$\%Error = \frac{C(V_{extreme}) - C(V_{opr})}{C(V_{opr})} \tag{4.16}$$

Substituting equations 4.14 and 4.12:

$$\%Error = \frac{(a-b)^2 - (a-1)^2}{(a-1)^2} \tag{4.17}$$

$$= \frac{(a-b)^2}{(a-1)^2} - 1 \tag{4.18}$$

Using the simulation data from Section 4.4, the average pressure at P2 corresponds to a $V_{opr}$ of 2.3e-4 $m^3$, and a 95$^{th}$ percentile compliance module pressure corresponds to $V_{extreme}$ of 2.76e-4 $m^3$. Setting a maximum allowable error of 5%, Equation 4.15 results in a $P_0$ of 81.4 kPa (11.8 psi). In order for this method to work, absolute pressure $P_0$ becomes the "ground" potential of the system. This means that the reservoir must also be pressurized (or evacuated) to $P_0$ in order to prevent the compliance module from blowing air though the system once the pump is powered off. While this is a solvable problem, the resulting module is more complicated and worse performing than the modules detailed below.

#### 4.5.1.2 Head Pressure Potential Field

An alternate design takes advantage of the pressure at the base of a water column. This is equivalent to storing potential energy by raising a rock on a rope and pulley system.

The equation for head pressure relates to the density of the fluid $\rho$, the acceleration due to gravity $g$, and the height of the water column $h$.

$$P = \rho g h \tag{4.19}$$

While "column" is generalized to mean the height of any continuous path of fluid in fluid dynamics, this module's design dictates that the fluid is stored in a simple vertical column with constant radius $r$ such that

$$h = \frac{V_C}{\pi r^2} \tag{4.20}$$

Substituting this expression for $h$ into equation 4.19 results in an equation for $P$ as a function of $V_C$

$$P = \frac{\rho g V_C}{\pi r^2} \tag{4.21}$$

Then, according to equation 4.4,

$$\frac{1}{C} = \frac{\partial P}{\partial V_C} = \frac{\rho g}{\pi r^2} \tag{4.22}$$

$$C = \frac{\pi r^2}{\rho g} \tag{4.23}$$

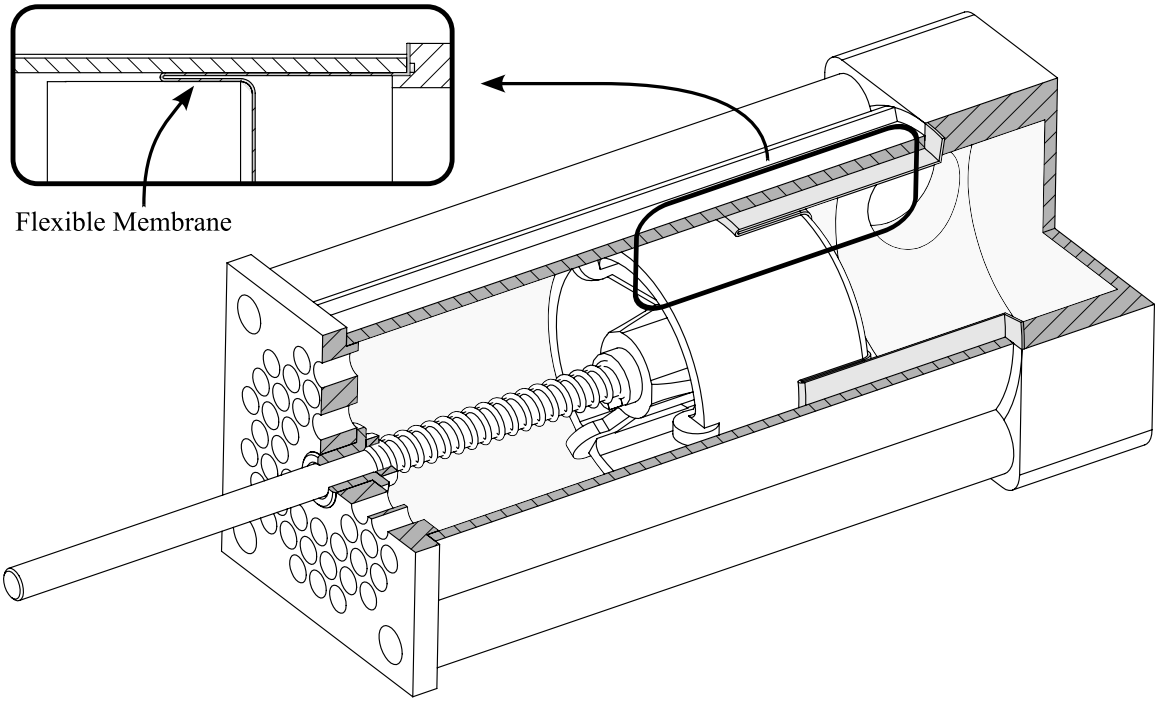


Figure 4.4: Schematic of the spring-and-piston compliance module

This expression for $C$ is not a function of $V_C$ which means that, unlike the air-spring system of Section 4.5.1.1, a module based on this design has the same compliance for any $V_C$.

For the compliance estimated by Sharp, Equation 4.21 dictates a tube with diameter 5/16". Unfortunately, the relative narrowness of the tube compared to the flow of fluid into the module introduced extraneous inertia dynamics. A prototype MCL with a compliance module of this design displayed dynamics that were unacceptably different from the desired Windkessel model. This design was ultimately ruled out due to these undesirable dynamics.

#### 4.5.1.3 Recommended Design: Spring-and-Piston Compliance

This work uses a pneumatic cylinder modified to contain an internal spring for its compliance module. A spring with spring constant $k$ exerts a force $F$ proportional to its deflection from rest $x$ such that

$$F = kx \tag{4.24}$$

If this spring is affixed to one side of a cylinder with radius $r$ and fluid is allowed to fill the other side, then

$$P = \frac{F}{\pi r^2} \tag{4.25}$$

$$x = \frac{V_C}{\pi r^2} \tag{4.26}$$

Combining all three equations results in an equation for $P$ as a function of $V_C$

$$P = \frac{V_C k}{\left(\pi r^2\right)^2} \tag{4.27}$$

Note that the pressure / volume relationship is not affected by the radius of the piston. For the sake of completeness, compliance is related to $k$ per equation 4.4

$$C = \frac{\left(\pi r^2\right)^2}{k} \tag{4.28}$$

Unsurprisingly, this expression for compliance is linear. In practice, however, friction between the piston and the cylinder walls negatively affects the linearity of this system. An early prototype using cup seals on the piston resulted in significant coulomb friction that interfered with the system dynamics.

The compliance module used in this work is based on a rolling diaphragm piston to minimize friction. This design is essentially a bag constrained by the cylinder walls and the piston. The bag inflates as fluid flows in which moves the piston. While the flexible barrier in true rolling diaphragm pistons have a special geometry to promote rolling, this system is able to use a bag of plastic film thin enough that negligible energy is lost to folding the bag.

### 4.5.2 Resistance Module Design

Fluid resistance measures the pressure drop across a pipe as a function of flow rate. For an incompressible working fluid with non-turbulent flow, the resistance of a fluid flowing through a pipe is governed by the Hagen-Poiseuille law:

$$R = 8\mu\pi l/A^2 \tag{4.29}$$

where $\mu$ is the viscosity of the working fluid, $l$ is the length of the pipe, and $A = \pi r^2$ is the cross-sectional area of a pipe with radius $r$. Having multiple channels is desirable to add another designable parameter. The

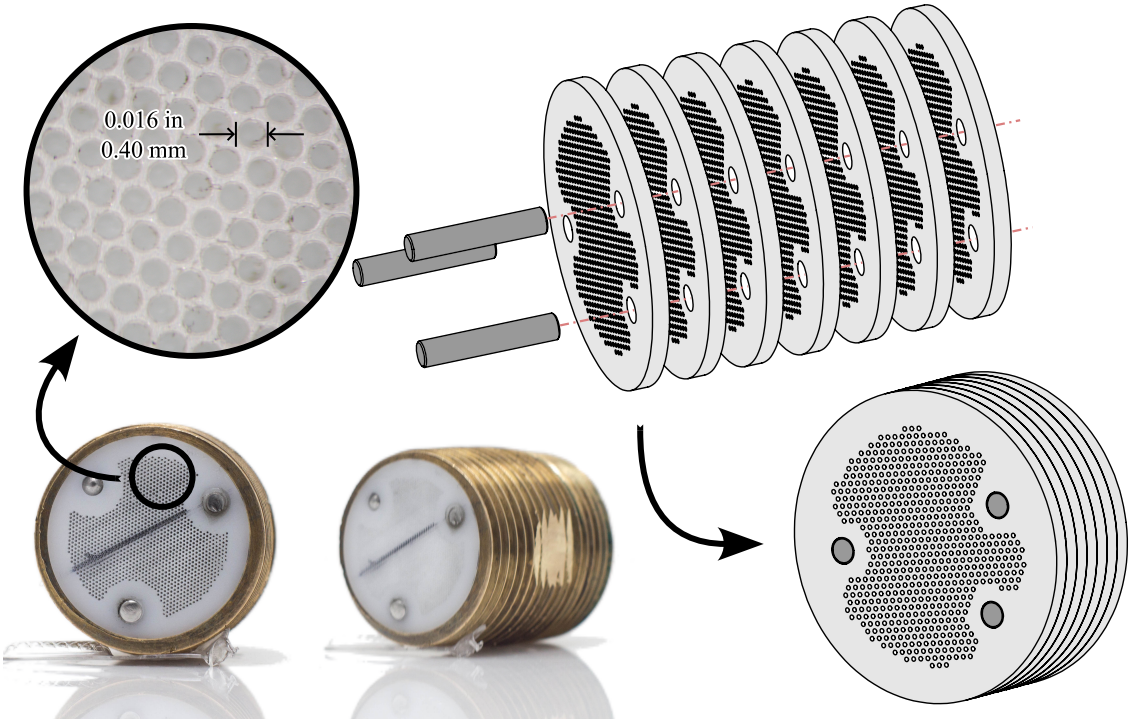


Figure 4.5: Photograph and Schematic of the Peripheral Resistance module fabricated in layers.

equivalent of $n$ resistances in parallel is the reciprocal of the sum of reciprocals.

$$R_{parallel} = (1/R_1 + 1/R_2 + \cdots + 1/R_n)^{-1} \tag{4.30}$$

$$= \frac{R}{n} \tag{4.31}$$

$$= \frac{8\mu\pi l}{nA^2} = \frac{8\mu\pi l}{(n\pi r^2)^2} \tag{4.32}$$

As this equation describes non-turbulent flow, the module design should keep the fluid's Reynolds number within the laminar region for the expected maximum flow rate $Q_{max}$:

$$Re = \frac{2\rho Q_{max}}{n\mu\pi r} < 2300 \tag{4.33}$$

Finally, channel radius and quantity are constrained by their packaging, that is, there are a limited number of channels that can fit inside a pipe's diameter. A constraint relating $n$ and $r$ is useful to limit potential designs by what is possible.

$$\pi r_{housing}^2 > 0.9069 n\pi \left(r + \frac{t}{2}\right)^2 \tag{4.34}$$

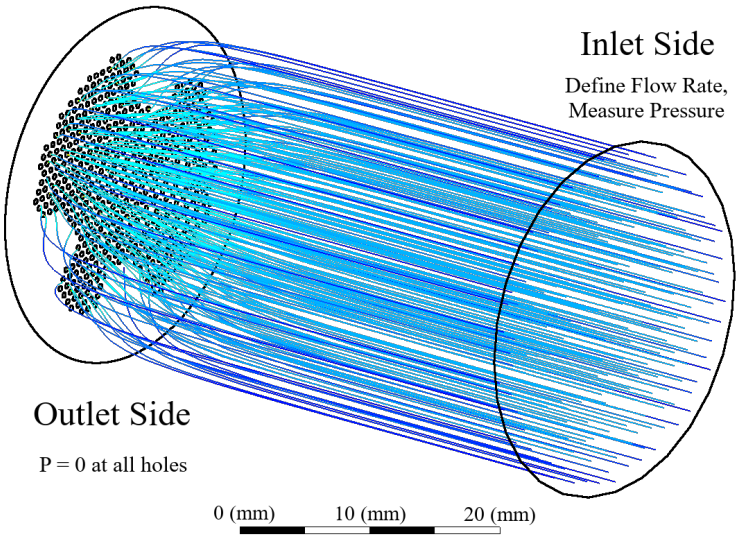


Figure 4.6: Streamlines of a Computational Fluid Dynamics model of the transition between pipes and orifices. Colors are not indicative of any quantity or intensity.

In this equation, $t$ is the minimum channel wall thickness a designer is willing to fabricate, and 0.9069 is densest packing factor possible for circles.

These three equations provide the constraints on the three design variables of this module, $r$, $n$, and $l$. While other works have used capillary tubes to build their flow channels, this work opts to use a stack of thin plastic wafers with drilled channels as seen in Figure 4.5. Acetal was the chosen material because it takes to machining operations well and is dimensionally stable even when submerged in water. This design allows for a more compact Peripheral Resistance Module compared to parallel capillary tubes as the channel wall thickness can be significantly smaller than packing tubes together. This also allows the designer to have more flexibility with the length of the channels, requiring only modifying a wafer thickness rather than trimming hundreds or thousands of individual tubes. The flexibility of the constraint Equations 4.33 and 4.34 allow for the use of standard sized drill bits while still achieving the desired flow resistance. The completed module is press fit into a brass nipple as seen in Figure 4.5B which allows for straight-forward swapping of different Peripheral Resistances.

### 4.5.3 Turbulent Flow and Effects on Resistances

While the flow restrictions are designed to keep the Reynolds Number within the laminar flow regime, the transition from a large flow channel to small flow channels is inherently turbulent. These transitions have nonlinear resistance associated with them that must be accounted for in the design of resistance modules.

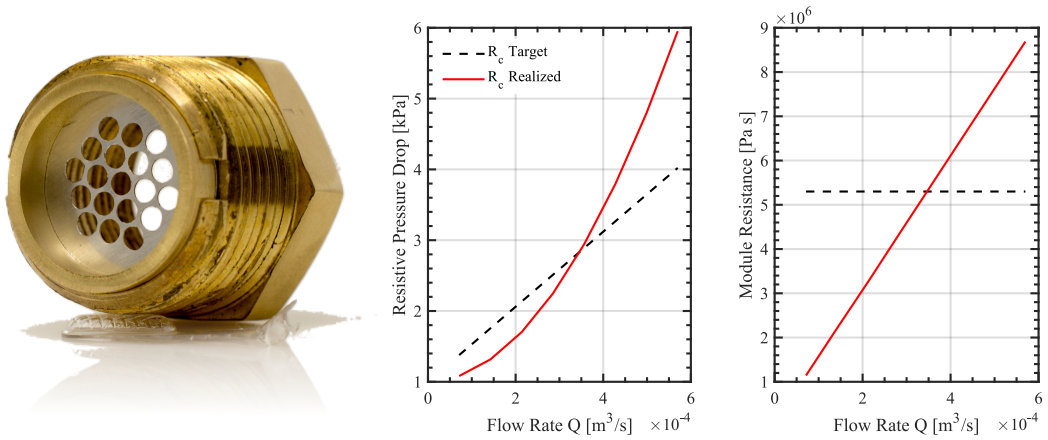


Figure 4.7: Photo of the Characteristic Resistance Module and plots of its simulated pressure drop and module resistance over the expected range of flow rates.

To quantify the transition resistance, fluid simulations of the flow leading up to the transition were built using ANSYS. Figure 4.6 shows a sample simulation setup with a single large inlet and multiple small outlets in the size and position of the restriction channels. A set of flow velocities corresponding to realistic heart volume flow rates was defined at the inlet and the resulting area averaged inlet pressure was recorded.

Figure 4.7 shows the transition resistance with respect to flow rates for the Characteristic Resistance module. These simulation results show that the transition resistance is proportional to flow, meaning that it is impossible to design a perfectly linear resistance to match the lumped parameter model. Therefore, the design of the Peripheral Resistance module is based around the lumped parameter $R_p$ less the transition resistance calculated at the average heart flow output. The Characteristic Resistance parameter is a similar order of magnitude to the transition resistance as seen in Figure 4.7. This means that while the Peripheral resistance module can be designed to minimize these nonlinear effects compared to the channel resistance, the Characteristic Resistance Module's resistance comes entirely from the transition resistance, and is non-linear.

Fluid simulations also show that the transition resistance is proportional to the "inactive" portion of the module, *i.e.*, the surface area perpendicular to the flow path that isn't holes. Note that fluid simulations show that this resistance is not affected by tapering the transition area. These results suggest that parallel channels should be packed into the available space as densely as possible to minimize the nonlinear effects of flow transition.

### 4.5.4 Inertance Module Design

A system's inertance can be thought of as it's "mass", or it's unwillingness to change flow. If the Characteristic Resistance can be a separate module, the Inertance Module is simple to design. The inertance of a fluid

in a pipe is

$$I = \rho l / A \tag{4.35}$$

where $\rho$ is the working fluid density, $l$ is the length of the pipe, and $A$ is the cross-sectional area. As this equation determines the ratio between $l$ and $A$, the specific values of these parameters are up to the designer. Note that $A$ should be sufficiently large as to minimize pipe resistance.

As described in Section 4.5.3, the Characteristic Resistance of the target parameter set is quite small, and can be handled in its own module. However, if the Characteristic Resistance is large, it may be necessary to design the Characteristic Resistance and the Inertance into the same module. Continuing along the same lines as Equation 4.32, the equivalent of $n$ parallel inertances is the reciprocal of the sum of reciprocals.

$$I_{parallel} = (1/I_1 + 1/I_2 + \cdots + 1/I_n)^{-1} \tag{4.36}$$

$$= \frac{I}{n} \tag{4.37}$$

$$= \frac{\rho l}{nA} \tag{4.38}$$

Since equations for resistance and inertance share both $A$ and $l$, a starting point for optimization can be found by solving equations 4.32 and 4.38 for $l$ and setting $l$ to be equivalent. This results in an equation defining $A$ for the ratio between $R$ and $I$.

$$A_{optimal} = \frac{8\pi\mu}{\rho}\frac{L}{R} \tag{4.39}$$

Note that $A_{optimal}$ is dependent only on the working fluid properties, $\mu$ and $\rho$, and the ratio of $I/R$, and not dependent on number of holes $n$. With a set $A$, Equations 4.33 and 4.34 can be used to determine $l$ and $n$.

### 4.6 Hardware Validation and Parameter Estimation

The Mock Circulatory Loop (MCL) pictured in 4.8A was fabricated and assembled according to the geometry defined in Table 4.2. The mock loops in literature use either a water glycerol solution mixed to acheive the viscosity and density of blood [56], or a standard Blood Mimicking Fluid (BMF), which has the same density, viscosity, and acoustic imaging properties as blood. The particulates in the BMF tend to clog the tiny orificies of the Peripheral Resistance Module, so this work uses a 0.430 glycerol to water mass ratio to achieve a viscosity of 4.0e-3 Pa s based on the equations in [57].

The schematic in Figure 4.8B shows the configuration of the MCL for parameter estimation. Two pressure sensors (Honeywell, Charlotte NC, USA) measure the pressure at the MCL input, P1, and the pressure at the compliance module, P2. This work uses a piston pump to provide the fluid flow to the system. The piston position is measured using an optical encoder (EM1 by US Digital, Vancouver WA, USA), which is related

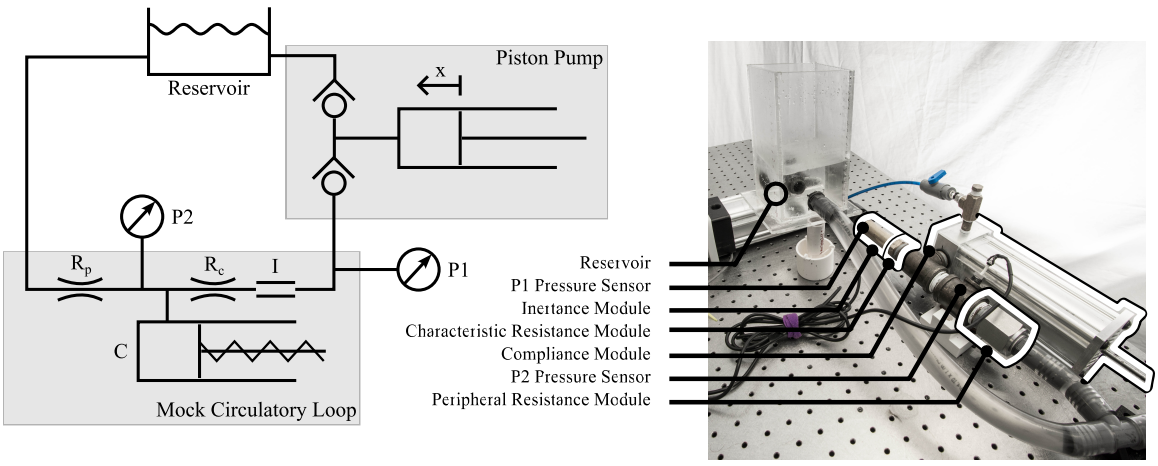


Figure 4.8: Simplified Schematic of the Mock Circulatory Loop System connected to a pump.

| Module | Target Parameter | Estimated Parameter | Units |
|---|---|---|---|
| Characteristic Resistance $R_c$ | 5.30e+6 | 3.48e+6 $\pm$ 0.04e+6 | Pa s $m^{-3}$ |
| Inertance $I$ | 3.12e+5 | 3.12e+5 $\pm$ 0.11e+5 | Pa $s^2$ $m^{-3}$ |
| Compliance $C$ | 1.77e-8 | 1.909e-8 $\pm$ 0.719e-8 | $m^3$ $Pa^{-1}$ |
| Peripheral Resistance $R_p$ | 1.22e+8 | 1.38e+8 $\pm$ 0.521e+8 | Pa s $m^{-3}$ |

Table 4.3: Final Parameter Estimates for the fabricated hardware

to flow rate $Q$ by the piston's cross-sectional area, $A$:

$$Q = \dot{x}A \quad when \quad \dot{x} > 0 \; and \; \ddot{x} > 0 \tag{4.40}$$

The piston pump with check valves introduced significant challenges in the parameter estimation, specifically that there are situations where the fluid inertia draws flow directly from the reservoir, resulting in un-metered flow into the system. The effects of this undesirable behavior on parameter estimation are mitigated by selecting data only where piston velocity and acceleration are positive, which is when the system flow is most likely coming from the piston pump alone.

Expressions directly relating $Q$, $P1$, and $P2$ in terms of the lumped parameters $R_c$, $I$, $C$, and $R_p$ can be found using the dynamic equations in 4.2.

$$P1 - P2 = I\dot{Q} + R_c Q \tag{4.41}$$

$$\begin{bmatrix} \frac{P1-P2}{(\tau s+1)^2} \end{bmatrix} = \begin{bmatrix} \frac{s}{(\tau s+1)^2} Q & \frac{1}{(\tau s+1)^2} Q \end{bmatrix} \begin{bmatrix} I \\ R_c \end{bmatrix} \tag{4.42}$$

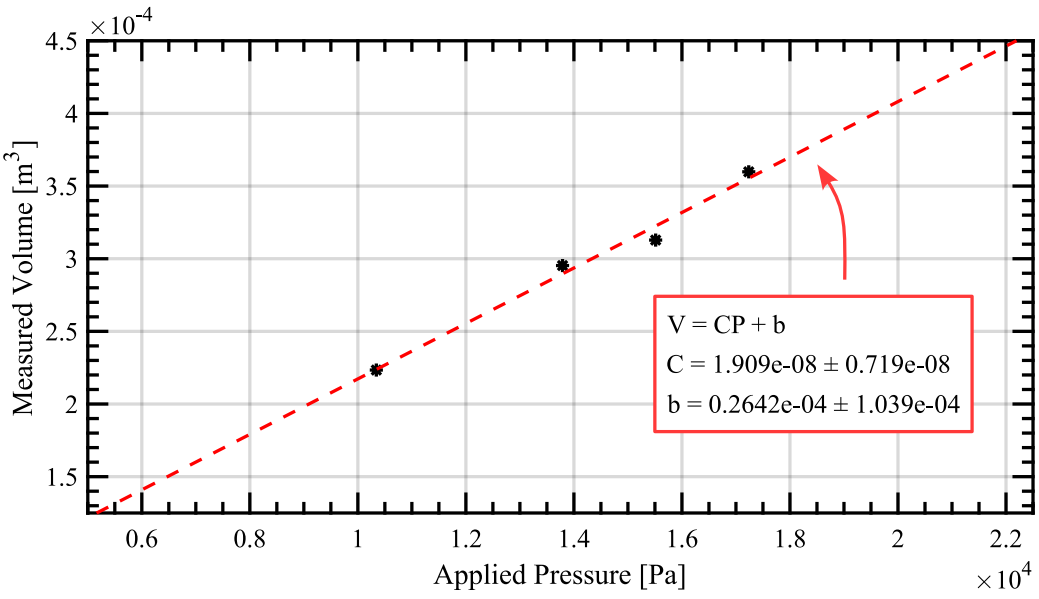


Figure 4.9: Plot of Pressure vs. Volume for the fabricated Compliance Module to measure its hydraulic compliance $C$

Both $P1-P2$ and $Q$ are filtered though transfer functions where the time constant *tau* determines the cutoff frequency for the filters. Matrices are constructed with filtered timeseries of $P1-P2$ and $Q$, allowing for the calculation of parameters $I$ and $R_c$ using overconstrained least squares. Since $Q$ is not directly measurable with the setup described above, Equation 4.40 is substituted in for $Q$.

$$\left[\frac{P1-P2}{(\tau s+1)^2}\right] = \left[\frac{s^2}{(\tau s+1)^2}Ax \quad \frac{s}{(\tau s+1)^2}Ax\right]\begin{bmatrix} I \\ R_c \end{bmatrix} \tag{4.43}$$

This results in the direct estimations of $I$ and $R_c$ found in Table 4.3. While the Inertance was estimated to be exactly that of the design, the estimated Characteristic Resistance is 34% lower than the designed value. This is likely due to the Characteristic Resistance module's resistance nonlinear behavior; the estimated parameter $R_c$ depends on the flow rate used for data collection. These parameters were estimated with an RMS $Q_in$ of 1.92e-4, which, according to Figure 4.7, corresponds to an expected Characteristic Resistance of 3.1e6. The estimate of 3.48e6 only differs 12% from this expected value.

The Compliance Module's parameter $C$ can be measured directly by applying a known pressure to the module and measuring the piston displacement. According to Equation 4.4, $C$ is the slope of volume with respect to applied pressure. For the data shown in Figure 4.9, the linear fit slope is the measured compliance $C$.

The equation of motion in Equation 4.2 shows that state P2, the pressure inside the compliance module,

depends only on itself and the flow into the system.

$$C\dot{P2} + R \cdot P2 = Q_{in} = 0 \tag{4.44}$$

The Compliance and Peripheral Resistance form a 1st order low-pass filter. This system has a distinct exponential decay behavior when unforced. Therefore, when no flow is entering the system, Equation 4.2 simplifies to

$$P2 = \frac{1}{R_p C s + 1} = \frac{1}{\tau s + 1} \tag{4.45}$$

$$\tau = R_p C \tag{4.46}$$

This differential equation solves to a simple exponential decay

$$P2(t) = ae^{-t/\tau} \tag{4.47}$$

whose derivative is

$$\dot{P2}(t) = -\frac{1}{\tau} ae^{-t/\tau} \tag{4.48}$$

$$= -\frac{1}{\tau} P(t) \tag{4.49}$$

Rearranging this equation allows for the estimation of $\tau$ using the pressure reading at P2

$$\frac{\dot{P2}}{P2} = -\frac{1}{\tau} = a \tag{4.50}$$

Figure 4.10 shows data for P2 and its derivative collected with the hardware along with the data that was selected for the estimate of $\tau$ in blue. $\tau$ is easily found with the previous equation, and it's uncertainty can be found using the uncertainty of $a$ and the uncertainty equation:

$$\Delta f(x) = \left.\frac{\partial f}{\partial x}\right|_{\bar{x}} \Delta x \tag{4.51}$$

$$\Delta \tau = \left.\frac{\partial \tau}{\partial a}\right|_{\bar{a}} \Delta a \tag{4.52}$$

$$= \left.\frac{1}{a^2}\right|_{a=0.378} 0.002 \tag{4.53}$$

$$= 0.014 \tag{4.54}$$

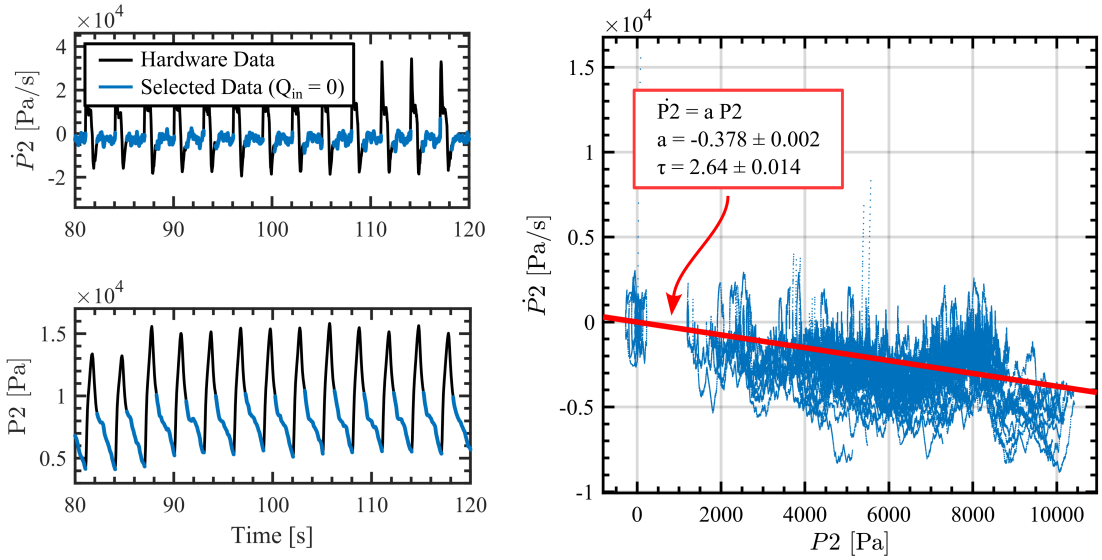


Figure 4.10: Plots of $P2$ and $\dot{P}2$ collected from hardware used to estimate the $R_pC$ time constant $\tau$.

Then, according to Equation 4.46 and based on $C$ estimated in 4.9, $R_P$ and its uncertainty is

$$R_p = \frac{\tau}{C} = 1.38e+8 \tag{4.55}$$

$$\Delta R_p = \sqrt{\left(\frac{\partial R_p}{\partial \tau}\Delta\tau\right)^2 + \left(\frac{\partial R_p}{\partial C}\Delta C\right)^2} \tag{4.56}$$

$$= \sqrt{\left(\frac{1}{C}\Delta\tau\right)^2 + \left(-\frac{\tau}{C^2}\Delta C\right)^2} \tag{4.57}$$

$$= 0.521e+8 \tag{4.58}$$

Overall, the estimated parameters of the full hardware system are remarkably close to the target parameters, meaning that the MCL is ready to test prototype artificial hearts, and that new modules to test pathological cases or patient-to-patient variability can be designed using the equations in Section 4.5.

## 4.7 Conclusion

The development of a Mock Circulatory Loop (MCL) for the testing of artificial hearts represents a much-needed stride in the advancement of cardiovascular engineering. This chapter has demonstrated the intricate process of design, fabrication, and validation of such a system, which will serve as an essential tool for the evaluation of artificial heart devices. By meticulously replicating a widely-accepted model of the human cardiovascular system in hardware, this work has created a platform that not only tests the controlability and endurance of prototype artificial hearts but also provides valuable insights into their performance under

diverse pathological scenarios.

The successful design and implementation of this mock circulatory loop have provided a foundation for future research and development of artificial heart technology. The versatile nature of the system allows for various parameters to be adjusted, enabling researchers to simulate a wide range of clinical situations and evaluate the response of artificial hearts. This system will allow researchers to fine tune their hardware prototypes and controller design with a realistic operating environment. to ensure their safety, reliability, and effectiveness.

As we move forward, the knowledge and experience gained from this research will continue to inform the design and development of artificial hearts, bringing us closer to the realization of safer and more efficient solutions for patients in need. The mock circulatory loop serves as a crucial stepping stone in this journey, offering a bridge between *in silico* simulations and clinical experiments. This chapter seeks to contribute to the ongoing efforts to improve the lives of individuals suffering from heart failure.

### 4.8 Future Directions

With the Mock Circulatory Loop assembled and parameters verified, the next step is to experiment with both positive displacement and pressure source pump styles to assess the advantages and challenges of their interactions with the circulatory system's inertence. Pressure spikes and troughs caused by changes in flow could cause damage to the aorta if left unchecked.

A positive displacement pump should have a check valve across its inlet and outlet ports to prevent the outlet pressure from going below the inlet pressure, possibly causing the aorta to collapse. To prevent harmful pressure spikes/troughs, it is recommended to generate a flow target by filtering the pressure target though the Inertence / Characteristic Resistance transfer function. As long as the controller has good reference following, this should ensure the pump's flow is smooth enough to prevent dangerous pressures while maximizing flow bandwidth.

A pressure source pump may be innately safer, as the pressure is directly controlled by the pump and its controller. This pump, however, will require a sensor to measure output flow rate to ensure the body is receiving sufficient blood flow for the activity level and potential pathological conditions. Recall that high blood pressure is the body's effort to compensate for pathological conditions causing insufficient flow. An artificial heart must also be capable of these modifications, and therefore must monitor flow.

Finally, if the MCL modules are frequently changed for multiple parameter sets, or if more advanced non-linear models are developed from clinical cardiac output data, it may be beneficial to design a fully controllable device that can match any dynamic impedance (impedance control). The Peripheral Resistance module will generate a pressure based on average flow rate, while a single powered piston can be used to

generate the pressures caused by the Inertence, Characteristic Resistance, and Compliance modules. Such a system will need a bandwidth higher than a candidate pump's dynamics to ensure that the interactions between the controllable MCL and the candidate pump are anatomically accurate.

# Appendix A

# LIST OF PUBLICATIONS

## A.1 Publications Relevant to Dissertation Work

**J. Howard**, S. Thomas, E. Barth, "Design and Evaluation of A Mock Circulatory Loop as a Dynamically Accurate Load for Artificial Heart Development", in ASAIO Journal, In Preparation.

**J. Howard**, C. Khan, B. Byram, J. Mitchell, "Scanning 3D Space with Mirrors: Design, Simulation, and Evaluation of an Elevational Focusing and Scanning Ultrasound Device Using Acoustic Mirrors," in IEEE Transactions on Ultrasonics, Ferroelectrics, and Frequency Control, In Preparation.

**J. Howard**, S. Thomas, C. Gallentine, and E. Barth, "Hydraulic Test Stand to Model Circulatory System Dynamics for Artificial Heart Evaluation," in BATH/ASME 2021 Symposium on Fluid Power and Motion Control, 2021.

**J. T. Howard**, E. J. Barth, R. D. Schrimpf, R. A. Reed, L. C. Adams, D. Vibbert, A. F. Witulski, "Methodology for Identifying Radiation Effects in Robotic Systems with Mechanical and Control Performance Variations," in IEEE Transactions on Nuclear Science, vol. 66, no. 1, pp. 184-189, Jan. 2019.

**J. T. Howard**, E. J. Barth, R. D. Schrimpf, R. A. Reed, D. Vibbert, A. F. Witulski, "Methodology for Identifying Radiation Effects in Robotic Systems with Mechanical and Control Performance Variations," IEEE Nuclear and Space Radiation Effects Conference (NSREC), July 2018.

## A.2 Other Publications

M. Li, Y. Chen, M. J. Slepian, **J. Howard**, S. Thomas, and E. J. Barth, "Design, Modeling, and Experimental Characterization of A Valveless Pulsatile Flow Mechanical Circulatory Support Device," J. Med. Device., vol. 15, no. 2, 2021, doi: 10.1115/1.4049560.

Y. Chen, S. T. Sengupta, **J. T. Howard**, "Closed Loop Control of an MR-conditional Robot Using Wireless Tracking Coil," Ann Biomed Eng, vol. 47, pp. 2322–2333 Jun 2019.

L. C. Adams, **J. Howard**, E. J. Barth, R. D. Schrimpf, R. A. Reed, R. A. Peters, A. F. Witulski, "Machine Learning Techniques for Mitigating Sensor Ionizing Dose Failures in Robotic Systems," IEEE Radiation Effects on Components and Systems, (RADECS), Sept. 2018.

## References


[1] Austria Microsystems, "AS5048A / AS5048B Magnetic Rotary Encoder (14-Bit Angular Position Sensor)," 2016.

[2] NAVSEA 00C3 Diving Program Division, "Requirements Document Diver's Augmented Visualization Device (DAVD)," tech. rep., 2014.

[3] NAVSEA 00C3 Diving Program Division, "Divers Augmented Vision Display Phase I Report," tech. rep., Naval Surface Warfare Center, Panama City Division, Panama City, Florida, 2016.

[4] National Center for Health Statistics, "Table 13," 2019.

[5] National Center for Health Statistics, "Table 5," 2019.

[6] N. Melton, B. Soleimani, and R. Dowling, "Current Role of the Total Artificial Heart in the Management of Advanced Heart Failure," 11 2019.

[7] B. Ji and A. Ündar, "An evaluation of the benefits of pulsatile versus nonpulsatile perfusion during cardiopulmonary bypass procedures in pediatric and adult cardiac patients," 7 2006.

[8] S. Kawatsuma, M. Fukushima, and T. Okada, "Emergency response by robots to Fukushima-Daiichi accident: Summary and lessons learned," Industrial Robot, vol. 39, no. 5, pp. 428–435, 2012.

[9] E. Strickland, "Fukushima's next 40 years," IEEE Spectrum, vol. 51, no. 3, pp. 46–53, 2014.

[10] M. Decréton, "Position sensing in nuclear remote operation," Measurement, vol. 15, no. 1, pp. 43–51, 1995.

[11] E. B. Pitt, E. J. Barth, Z. J. Diggins, N. Mahadevan, G. Karsai, B. D. Sierawski, R. A. Reed, R. D. Schrimpf, R. A. Weller, M. L. Alles, and A. F. Witulski, "Radiation Response and Adaptive Control-Based Degradation Mitigation of MEMS Accelerometers in Ionizing Dose Environments," IEEE Sensors Journal, vol. 17, no. 4, pp. 1132–1143, 2017.

[12] Z. J. Diggins, N. Mahadevan, E. B. Pitt, D. Herbison, R. M. Hood, G. Karsai, B. D. Sierawski, E. J. Barth, R. A. Reed, R. D. Schrimpf, R. A. Weller, M. L. Alles, and A. F. Witulski, "Bayesian Inference Modeling of Total Ionizing Dose Effects on System Performance," IEEE Transactions on Nuclear Science, vol. 62, no. 6, pp. 2517–2524, 2015.

[13] Z. J. Diggins, N. Mahadevan, D. Herbison, G. Karsai, E. Barth, R. A. Reed, R. D. Schrimpf, R. A. Weller, M. L. Alles, and A. Witulski, "Range-finding sensor degradation in gamma radiation environments," IEEE Sensors Journal, vol. 15, no. 3, pp. 1864–1871, 2015.

[14] C. Laa and S. Larsson, "TID and SEU testing of Hall effect Sensor," in European Space Agency, (Special Publication) ESA SP, vol. 2003-Septe, pp. 567–570, 2003.

[15] A. B. Sanders, H. S. Kim, and A. Phan, "TID and SEE Response of Optek Hall Effect Sensors," pp. 148–151, 2008.

[16] P. Adamiec, J. Barbero, E. Cordero, P. Dainesi, and N. Steiner, "Radiation Hard Contactless Angular Position Sensor Based on Hall Effect," IEEE Transactions on Nuclear Science, vol. 63, no. 6, pp. 2971–2978, 2016.

[17] C. H. Brase and C. P. Brase, Understandable statistics : concepts and methods. Lexington, Mass.: D.C. Heath, 1991.

[18] S. J. Kline and F. A. McClintock, "Uncertainties in single-sample experiments," Mechanical Engineering, vol. 75, pp. 3–8, 1953.

[19] S. Chen, B. Liu, C. Feng, C. Vallespi-Gonzalez, and C. Wellington, "3D Point Cloud Processing and Learning for Autonomous Driving: Impacting Map Creation, Localization, and Perception," IEEE Signal Processing Magazine, vol. 38, pp. 68–86, 1 2021.

[20] Z. Farid, R. Nordin, and M. Ismail, "Recent advances in wireless indoor localization techniques and system," Journal of Computer Networks and Communications, vol. 2013, 2013.

[21] L. Paull, S. Saeedi, M. Seto, and H. Li, "AUV navigation and localization: A review," IEEE Journal of Oceanic Engineering, vol. 39, pp. 131–149, 1 2014.

[22] E. O. Belcher, W. L. Fox, and W. H. Hanot, "Dual-frequency acoustic camera: A candidate for an obstacle avoidance, gap-filler, and identification sensor for untethered underwater vehicles," in Oceans Conference Record (IEEE), vol. 4, pp. 2124–2128, 2002.

[23] D. Cook, K. Middlemiss, P. Jaksons, W. Davison, and A. Jerrett, "Validation of fish length estimations from a high frequency multi-beam sonar (ARIS) and its utilisation as a field-based measurement technique," Fisheries Research, vol. 218, pp. 59–68, 10 2019.

[24] F. Bonnin-Pascual and A. Ortiz, "On the use of robots and vision technologies for the inspection of vessels: A survey on recent advances," Ocean Engineering, vol. 190, p. 106420, 10 2019.

[25] J. Helminen and T. Linnansaari, "Object and behavior differentiation for improved automated counts of migrating river fish using imaging sonar data," Fisheries Research, vol. 237, p. 105883, 5 2021.

[26] C. L. Epifanio, J. R. Potter, G. B. Deane, M. L. Readhead, and M. J. Buckingham, "Imaging in the ocean with ambient noise: the ORB experiments," The Journal of the Acoustical Society of America, vol. 106, pp. 3211–3225, 11 1999.

[27] X. Zhang, Y. Liu, C. Tao, J. Yin, Z. Hu, S. Yuan, Q. Liu, and X. Liu, "High-sensitivity optical-resolution photoacoustic microscopy with an optical-acoustic combiner based on an off-axis parabolic acoustic mirror," Photonics, vol. 8, no. 4, 2021.

[28] Z. Dong, G. Student Member, S. Li, X. Duan, M. R. Lowerison, C. Huang, Q. You, S. Chen, S. Member, J. Zou, and P. Song, "High Volume Rate 3-D Ultrasound Imaging Using Fast-Tilting and Redirecting Reflectors,"

[29] L. Mordfin, Handbook of Reference Data for NonDestructive Testing. Baltimore, MD: ASTM, 2002.

[30] T. L. Szabo, Diagnostic Ultrasound Imaging: Inside Out. 2004.

[31] L. Demi, "Practical guide to ultrasound beam forming: Beam pattern and image reconstruction analysis," Applied Sciences (Switzerland), vol. 8, no. 9, 2018.

[32] A. Ng and J. Swanevelder, "Resolution in ultrasound imaging," Continuing Education in Anaesthesia, Critical Care and Pain, vol. 11, pp. 186–192, 10 2011.

[33] B. E. Treeby, J. Jaros, D. Rohrbach, and B. T. Cox, "Modelling elastic wave propagation using the k-Wave MATLAB Toolbox," in IEEE International Ultrasonics Symposium, IUS, pp. 146–149, 2014.

[34] N. Moazami, W. P. Dembitsky, R. Adamson, R. J. Steffen, E. G. Soltesz, R. C. Starling, and K. Fukamachi, "Does pulsatility matter in the era of continuous-flow blood pumps?," 2015.

[35] P. M. Eckman and R. John, "Bleeding and thrombosis in patients with continuous-flow ventricular assist devices," Circulation, vol. 125, pp. 3038–3047, 6 2012.

[36] A. M. Patel, G. A. Adeseun, I. Ahmed, N. Mitter, J. Eduardo Rame, and M. R. Rudnick, "Renal failure in patients with left ventricular assist devices," 3 2013.

[37] A. L. Meyer, C. Kuehn, J. Weidemann, D. Malehsa, C. Bara, S. Fischer, A. Haverich, and M. Strüber, "Thrombus formation in a HeartMate II left ventricular assist device," Journal of Thoracic and Cardiovascular Surgery, vol. 135, no. 1, pp. 203–204, 2008.

[38] A. S. Bryant, W. L. Holman, N. C. Nanda, S. Vengala, M. S. Blood, S. V. Pamboukian, and J. K. Kirklin, "Native aortic valve insufficiency in patients with left ventricular assist devices," Annals of Thoracic Surgery, vol. 81, no. 2, 2006.

[39] S. Crow, R. John, A. Boyle, S. Shumway, K. Liao, M. Colvin-Adams, C. Toninato, E. Missov, M. Pritzker, C. Martin, D. Garry, W. Thomas, and L. Joyce, "Gastrointestinal bleeding rates in recipients of nonpulsatile and pulsatile left ventricular assist devices," Journal of Thoracic and Cardiovascular Surgery, vol. 137, no. 1, pp. 208–215, 2009.

[40] S. Crow, D. Chen, C. Milano, W. Thomas, L. Joyce, V. Piacentino, R. Sharma, J. Wu, G. Arepally, D. Bowles, J. Rogers, and N. Villamizar-Ortiz, "Acquired von Willebrand syndrome in continuous-flow ventricular assist device recipients," Annals of Thoracic Surgery, vol. 90, no. 4, pp. 1263–1269, 2010.

[41] J. Wappenschmidt, S. J. Sonntag, M. Buesen, S. Gross-Hardt, T. Kaufmann, T. Schmitz-Rode, R. Autschbach, and A. Goetzenich, "Fluid Dynamics in Rotary Piston Blood Pumps," Annals of Biomedical Engineering, vol. 45, pp. 554–566, 3 2017.

[42] M. Li and E. Barth, "Spherical Gerotor: Synthesis of a Novel Valveless Pulsatile Flow Spherical Total Artificial Heart," Journal of Mechanics Engineering and Automation, vol. 8, 7 2018.

[43] M. Li, Y. Chen, M. J. Slepian, J. Howard, S. Thomas, and E. J. Barth, "Design, Modeling, and Experimental Characterization of A Valveless Pulsatile Flow Mechanical Circulatory Support Device," Journal of Medical Devices, vol. 15, no. 2, 2021.

[44] N. Westerhof, J.-W. Lankhaar, and B. E. Westerhof, "The arterial Windkessel," Medical & Biological Engineering & Computing, vol. 47, pp. 131–141, 2 2009.

[45] O. Frank, "The basic shape of the arterial pulse. First treatise: Mathematical analysis," Journal of Molecular and Cellular Cardiology, vol. 22, pp. 255–277, 3 1990.

[46] D. K. Hildebrand, Z. J. Wu, J. E. Mayer, and M. S. Sacks, "Design and hydrodynamic evaluation of a novel pulsatile bioreactor for biologically active heart valves," Annals of Biomedical Engineering, vol. 32, no. 8, pp. 1039–1049, 2004.

[47] N. Westerhof, G. Elzinga, and P. Sipkema, "An artificial arterial system for pumping hearts.," Journal of applied physiology, vol. 31, no. 5, pp. 776–781, 1971.

[48] E. O. Kung and C. A. Taylor, "Development of a Physical Windkessel Module to Re-Create In Vivo Vascular Flow Impedance for In Vitro Experiments," Cardiovascular Engineering and Technology, vol. 2, no. 1, pp. 2–14, 2011.

[49] H. Huang, M. Yang, W. Zang, S. Wu, and Y. Pang, "In vitro identification of four-element windkessel models based on iterated unscented kalman filter," IEEE Transactions on Biomedical Engineering, vol. 58, no. 9, pp. 2672–2680, 2011.

[50] N. Stergiopulos, B. E. Westerhof, and N. Westerhof, "Total arterial inertance as the fourth element of the windkessel model," American Journal of Physiology-Heart and Circulatory Physiology, vol. 276, pp. H81–H88, 1 1999.

[51] M. K. Sharp and R. K. Dharmalingam, "Development of a hydraulic model of the human systemic circulation," 1999.

[52] R. Burattini and P. O. Di Salvia, "Development of systemic arterial mechanical properties from infancy to adulthood interpreted by four-element windkessel models," Journal of Applied Physiology, vol. 103, no. 1, pp. 66–79, 2007.

[53] W. W. Nichols, C. R. Conti, W. E. Walker, and W. R. Milnor, "Input impedance of the systemic circulation in man," Circulation Research, vol. 40, no. 5, pp. 451–458, 1977.

[54] J. P. Murgo, N. Westerhof, J. P. Giolma, and S. A. Altobelli, "Aortic input impedance in normal man: relationship to pressure wave forms.," Circulation, vol. 62, no. 1, pp. 105–116, 1980.

[55] A. S. Les, S. C. Shadden, C. A. Figueroa, J. M. Park, M. M. Tedesco, R. J. Herfkens, R. L. Dalman, and C. A. Taylor, "Quantification of hemodynamics in abdominal aortic aneurysms during rest and exercise using magnetic resonance imaging and computational fluid dynamics," Annals of Biomedical Engineering, vol. 38, no. 4, pp. 1288–1313, 2010.

[56] S. Boës, G. Ochsner, R. Amacher, A. Petrou, M. Meboldt, and M. Schmid Daners, "Control of the Fluid Viscosity in a Mock Circulation," Artificial Organs, vol. 42, pp. 68–77, 1 2018.

[57] N.-S. Cheng, "Formula for the Viscosity of a Glycerol-Water Mixture," Industrial & Engineering Chemistry Research, vol. 47, pp. 3285–3288, 5 2008.